



An improved inertial/wifi/magnetic fusion structure for indoor navigation



You Li^{a,b}, Yuan Zhuang^{a,*}, Peng Zhang^b, Haiyu Lan^a, Xiaoji Niu^b, Naser El-Sheimy^a

^a Department of Geomatics Engineering, University of Calgary, 2500 University DR NW Calgary, T2N 1N4, Canada

^b GNSS Research Center, Wuhan University, 129 Luoyu Road, Wuhan, 430079, P.R. China

ARTICLE INFO

Article history:

Received 10 June 2015

Revised 20 May 2016

Accepted 19 June 2016

Available online 21 July 2016

Keywords:

Indoor pedestrian navigation

Mems sensors

Portable devices

Wireless positioning

Magnetic feature

ABSTRACT

This paper proposes a dead-reckoning (DR)/WiFi fingerprinting/magnetic matching (MM) integration structure that uses off-the-shelf sensors in consumer portable devices and existing WiFi infrastructures. One key improvement of this structure over previous DR/WiFi/MM fusion structures is the introduction of a three-level quality-control (QC) mechanism based on the interaction between different techniques. On QC Level #1, several criteria are applied to filter out blunders or unreliable measurements in each separate technology. Then, on Level #2, a threshold-based approach is used to set the weight of WiFi results automatically through the investigation of the EKF innovation sequence. Finally, on Level #3, DR/WiFi results are utilized to limit the MM search space and in turn reduce both mismatch rate and computational load. The proposed structure reduced the root mean square (RMS) of position errors in the range of 13.3 to 55.2% in walking experiments with two smartphones, under four motion conditions, and in two indoor environments. Furthermore, the proposed structure reduced the rate of mismatches (i.e., matching to an incorrect point that is geographically located over 15 m away from the true position) rate by over 75.0% when compared with previous DR/WiFi/MM integration structures.

© 2016 Elsevier B.V. All rights reserved.

1. Introduction

Indoor pedestrian navigation (i.e., determination of position, velocity, and attitude) is increasingly important due to their potential applications in a wide range of mobile location-based services (LBS) from emergency responders to commercial advertising and social networks [1,2]. Most LBS users spend 70 - 90% of their time in indoor or urban areas [3]. Thus, a trustworthy indoor navigation solution is highly demanding [4].

While Global Navigation Satellite Systems (GNSS) based outdoor navigation has greatly advanced over the past decades, positioning indoors is still an open issue [5]. The challenges include the unavailability or degradation of GNSS signals, the complexity of indoor environments, the necessity of using low-grade devices, etc. Various indoor positioning technologies based on Radio Frequency (RF) signals have been researched, such as IEEE 802.11 WLAN (WiFi), Radio Frequency identification (RFID) tags, ZigBee, Ultra Wideband Beacons (UWB), Bluetooth Low Energy (BLE), and pseudolites [6]. RF-based technologies can provide long-term absolute positions, but require the creation and maintenance of a network [7]. As WiFi chips become ubiquitous, positioning with ex-

isting WiFi infrastructures in public buildings becomes feasible [8]. WiFi fingerprinting approaches based on received signal strength (RSS) have gained a large amount of attention, as they can provide position without any knowledge of access point (AP) locations or radio propagation models [9]. Nevertheless, there are challenges for reaching high positioning accuracy by using WiFi RSS: a) the performance of a wireless positioning system depends on signal availability and geometry [10]. Weak geometry may lead to ambiguity problems [11]. b) The positioning performance is limited by RSS fluctuations caused by obstructions, reflections [12], and multipath effects [13]. Additionally, c) WiFi chips in smartphones are low-cost and have large signal diversity [14]. These issues have limited the promotion of WiFi and other wireless positioning techniques.

Advances in Micro-Electro-Mechanical Systems (MEMS) technology have made it possible to produce chip-based sensors, such as inertial sensors (i.e., accelerometers and gyros) and magnetometers. MEMS inertial sensors have been widely used in motion tracking and navigation applications because they are small size and light weight, and power saving [15]. For consumer portable devices, dead-reckoning (DR, by using either the inertial navigation system (INS) mechanism or pedestrian dead-reckoning (PDR)) is usually the algorithm used to navigate with inertial sensors; thus, inertial sensors are independent on the transmission or reception

* Corresponding author. Fax: (403) 284 1980.

E-mail address: zhy.0908@gmail.com (Y. Zhuang).

of signals from an external source [16]. The shortcoming is that inertial sensors provide only short-term accuracy and suffer from accuracy degradation over time due to the existence of sensor errors [17]. Calibration is useful to remove many deterministic sensor errors [18]; however, low-cost MEMS inertial sensors suffer from significant run-to-run biases and thermal drifts [19]. Residual sensor errors will accumulate and lead to navigation errors due to the integration process in the INS mechanization. Although the horizontal attitude errors can be controlled by accelerometer measurements, the heading error will grow when there is no aiding information [20]. Magnetometers can provide an absolute heading through leveling using accelerometers, magnetic heading calculation, and true heading computation [21]. However, this approach is developed based on the assumption that the local magnetic field (LMF) is mainly the geomagnetic field and thus the declination angle can be obtained from the International Geomagnetic Reference Field (IGRF) model [22]. Preliminary results indicated that the majority of outdoor tests met this assumption; however, the LMF was susceptible to magnetic interferences from man-made infrastructures in indoor areas. The existence of magnetic interferences is a critical issue when using magnetometers as a compass indoors [23].

The existence of indoor magnetic interferences can also be exploited as an advantage by leveraging the magnetic abnormalities as fingerprints or landmarks [24]. The magnetic matching (MM) approach has been proposed based on the hypothesis that the indoor magnetic field is stable over time and non-uniform (i.e., changes significantly) with location [25]. While MM utilizes a similar idea as WiFi fingerprinting, it has two advantages [25]: a) it is independent from any infrastructure as the magnetic field is omnipresent; and b) magnetometers have higher sampling rates. The challenge for MM is that magnetic data only consists of three components. Because heading is generally unknown, it is only feasible to extract two components (i.e., vertical and horizontal magnetic intensities, or total magnetic intensity and inclination). To increase magnetic fingerprint dimension without extra sensors, the profile-matching approach has been proposed [26]. A sequence of observations is saved in the memory and then compared with candidate profiles in a database. Profile-matching has been used in high-end self-contained terrain [27], gravity [28], and magnetic referenced navigation systems [29]; in addition, there are well-developed profile-matching methods such as terrain contour matching (TERCOM) [27] and iterative closest contour point (ICCP) [28]. However, the performance of MM is highly dependent on the LMF: MM solutions can be accurate but suffered from mismatches on some occasions, as there are hundreds of trajectories that have the similar magnetic features on the Earth.

Thus, all the existing indoor positioning technologies have advantages and disadvantages [30]. Considering their complementary characteristics, multi-sensor integration is a key factor of success for accurate and reliable navigation solutions. Because DR, WiFi, and MM are technologies that are available by using off-the-shelf sensors in consumer portable devices, their integration is investigated in this paper.

There is literature that focuses on enhancing navigation results through better fusion of inertial sensors and magnetometers. For example, the research [31] utilizes gyro-derived heading to detect severe magnetic disturbances, and the research [32] uses magnetometer measurements during quasi-static magnetic field (QSMF) periods to calibrate gyros. These approaches are effective on improving the robustness of DR, but still suffer from the issue inherent in DR – drifts of position. To provide long-term accuracy, a common approach is to integrate DR with absolute positioning techniques (e.g., WiFi). Different estimation techniques (e.g., Kalman filter [33] and particle filter [34]) have been used for information fusion. The majority of literature integrates DR with

wireless technologies through a loosely-coupled way [33], while some apply a tightly-coupled approach [35]. Compared with DR and WiFi, the research of indoor MM started later and most of related works are on the independent use of MM [36] or the integration of MM and DR [37]. For WiFi and MM, the research [38] and [39] integrate these technologies for indoor pedestrian navigation. The former uses a region-point indoor localization approach, while the latter applies a two-pass particle filter to fuse magnetic and WiFi signals. The literature [40] compares the region-point indoor localization approach and the approach that regards the magnetic intensity and inclination as pseudo WiFi APs.

For the integration of DR, WiFi, and MM, the literature [41] uses a Kalman filter to fuse the information from different sensors, while the research [42] utilizes a bundle adjustment approach to implement simultaneous localization and mapping. The hybrid navigation structure (named as Structure #0 in this paper) behind these works is to feed all sensor data into a fusion module. DR is used to provide continuous position predictions and build the system model; meanwhile, WiFi and MM positioning results are utilized directly as position updates.

Furthermore, scholars have noticed that MM results have small fluctuations [38], but have a risk of mismatching due to low magnetic fingerprint dimension [36]; in contrast, WiFi results have a low mismatch rate but suffer from larger fluctuations [40] (The term “mismatch rate” means “the percentage of position results that have a position error of over 15 m”). Therefore, there is a potential to use WiFi for a rough positioning, and then use MM for a more precise localization [38]. Thus, an improved structure (named as Structure #1 in this paper) can be developed. WiFi results are used to limit the MM search space. Afterwards, both WiFi and MM (WiFi aided) results are utilized as updates to correct DR. Tests in this paper supported that WiFi-aided MM could provide better results than either the independent use of WiFi or MM. Consequently, Structure #1 provided more reliable solutions than Structure #0. However, there were still mismatches in MM (WiFi aided) results because fluctuations of WiFi results is the issue inherent in approaches based on RSS. Therefore, an improved structure is presented in this paper to further improve the reliability of the hybrid DR/WiFi/MM navigation. In this paper, the sign “/” represents the integration of different techniques.

By using the same data from sensors and WiFi, different information fusion structures may lead to various results in Engineering practice. This paper first investigates on the independent use of DR, WiFi, and MM to indicate their advantages and disadvantages, and then optimizes the DR/WiFi/MM integration structure. The proposed structure first uses DR to provide continuous position predictions and calculates WiFi and MM positioning results as potential updates, which is similar to traditional integration structures. Afterwards, it integrates DR with WiFi, and utilizes DR/WiFi results to determine the MM search space. Accordingly, a three-level quality-control (QC) mechanism is proposed to enhance the system robustness in the above steps. This paper enhances the use of DR and MM as follows:

- A two-filter algorithm is utilized to enhance DR. The algorithm is comprised of an INS-based attitude-determination Extend Kalman filter (EKF) and a PDR-based position-tracking EKF. Multiple constraints are used to assure the algorithm works under natural phone motions such as handheld, phoning (i.e., close to the ear), dangling (i.e., walking with phone in hand), and pocketed (i.e., in a pants pocket).
- Several approaches are used to improve MM. For example, (a) Dynamic Time Warping (DTW) is used to match time-series with inaccurate profile lengths. (b) k-nearest neighbor (k-NN) is introduced from WiFi fingerprinting into MM. Finally, (c) both magnetic-gradient and magnetic-intensity fingerprints are uti-

lized to mitigate the effect of hardware diversities of magnetometers in mobile devices.

On the information fusion level, the navigation algorithm should be intelligent enough to set the weight of WiFi and MM position updates and filter out their mismatches automatically. Thus, a three-level QC mechanism is designed:

- On QC Level #1, several criteria are applied to remove blunders or unreliable measurements in each separate technology.
- On QC Level #2, a threshold-based method is used to set the weight of WiFi results through the investigation of the EKF innovation sequence (i.e., the difference between position predicted by DR and that measured by WiFi).
- On QC Level #3, DR/WiFi results are utilized to limit the MM search space and in turn reduce both mismatch rate and computational load.

The WiFi and MM results that have passed the QC mechanism are used as updates to further enhance the navigation performance.

Furthermore, this research implemented more comprehensive tests than previous literature that focuses on the handheld condition and assumes that the initialization of position and heading has been completed before navigation. Specifically,

- The proposed DR/WiFi/MM structure was compared with two previous structures by using two smartphones, under four motion conditions, and in two environments.
- The tests were designed through the consideration of challenging issues in indoor pedestrian navigation, including the initialization of navigation, the changes of motion conditions, and the timeliness of databases.
- Besides accuracy, this research introduced another indicator, i.e., the mismatch rate, to evaluate the reliability of navigation solutions, as reliability is strongly related with user experience in mass-market applications.
- Based on results from three groups of tests, performances of nine navigation strategies (i.e., one single technique or a combination of different techniques) were evaluated. Several unexpected outcomes were observed, for example:
- Accuracy and mismatch rate are related with one another, but are not exactly the same. That is, a navigation strategy that had a smaller root mean square (RMS) value of position errors than other techniques might suffer from a larger mismatch rate.
- Using more technologies could be an effective way to enhance navigation; however, the introduction of more technologies might increase the risk of mismatches and degrade the robustness of the system. This fact highlighted the importance of a reliable integration structure.

This paper is organized as follows: [Section 2](#) provides the methodology, including DR, WiFi fingerprinting, MM, and structures for their integration; [Section 3](#) explains details of tests and parameter settings; [Section 4](#) shows results and discussions, and [Section 5](#) draws the conclusions.

2. Methodology

This research focuses on two-dimensional walking applications. The navigation algorithm is comprised an attitude-determination EKF and a position-tracking EKF, which are introduced in Sections 2.1 and 2.2, respectively. [Section 2.3](#) provides details about WiFi fingerprinting and MM, while [Section 2.4](#) explains different DR/WiFi/MM Integration Structures.

2.1. INS-based attitude-determination EKF

Compared with the traditional PDR algorithm, the attitude-determination EKF is used to determine the heading under various motion conditions. The attitude-determination algorithm is comprised of the INS mechanization and EKF models. Refer to [43] and [44] for details about the INS mechanization and EKF, respectively. The following subsections introduce the system model and measurement model of the EKF.

2.1.1. Attitude-determination EKF system model

A simplified form of the INS error model is applied as the continuous-time state equations in the EKF [45].

$$\begin{bmatrix} \delta\dot{\mathbf{r}}^n \\ \delta\mathbf{v}^n \\ \dot{\psi} \\ \dot{\mathbf{b}}_g \\ \dot{\mathbf{b}}_a \end{bmatrix} = \begin{bmatrix} -\omega_{ie}^n \times \delta\mathbf{r}^n + \delta\mathbf{v}^n \\ -(2\omega_{ie}^n + \omega_{en}^n) \times \delta\mathbf{v}^n + \mathbf{f}^n \times \psi + \mathbf{C}_b^n(\mathbf{b}_a + \mathbf{w}_a) \\ -(\omega_{ie}^n + \omega_{en}^n) \times \psi - \mathbf{C}_b^n(\mathbf{b}_g + \mathbf{w}_g) \\ -(1/\tau_{bg})\mathbf{b}_g + \mathbf{w}_{bg} \\ -(1/\tau_{ba})\mathbf{b}_a + \mathbf{w}_{ba} \end{bmatrix} \quad (1)$$

where the states $\delta\mathbf{r}^n$, $\delta\mathbf{v}^n$ and ψ , \mathbf{b}_g , and \mathbf{b}_a are the vectors of position errors, velocity errors, attitude errors, gyro biases, and accelerometer biases, respectively; \mathbf{C}_b^n is the direction cosine matrix from the body frame (i.e., b-frame) to the navigation frame (i.e., n-frame) predicted by the INS mechanization; \mathbf{f}^n is the specific force vector projected to the n-frame, and ω_{ie}^n and ω_{en}^n represent the angular rate of the Earth and that of the n-frame with respect to the Earth-Centered Earth-Fixed frame (i.e., e-frame); \mathbf{w}_g and \mathbf{w}_a are sensor noises; τ_{bg} and τ_{ba} denote for the correlation time of sensor biases; \mathbf{w}_{bg} and \mathbf{w}_{ba} are the driving noises. The symbol “ \times ” denotes the cross product of two vectors.

If the pseudo-observations in the next subsection are not used, the Kalman filter system model can be simplified as

$$\begin{bmatrix} \dot{\psi} \\ \dot{\mathbf{b}}_g \end{bmatrix} = \begin{bmatrix} -(\omega_{ie}^n + \omega_{en}^n) \times \psi - \mathbf{C}_b^n(\mathbf{b}_g + \mathbf{w}_g) \\ -(1/\tau_{bg})\mathbf{b}_g + \mathbf{w}_{bg} \end{bmatrix} \quad (2)$$

2.1.2. Attitude-determination EKF measurement model

Various constraints are used to build the measurement model, including the pseudo-observations, accelerometer and magnetometer measurements as well as their normal vectors.

(a) Pseudo-observations

The pseudo-position and pseudo-velocity observations are proposed assuming that the ranges of the device's position and linear velocity are within a limited scope during the time periods between adjacent inertial sensor sampling time epochs [45]. Pseudo-position updates are used under natural pedestrian motion conditions in this paper:

$$\mathbf{r}^n - \tilde{\mathbf{r}}^n = \delta\mathbf{r}^n + \mathbf{n}_1 \quad (3)$$

where $\mathbf{r}^n = \mathbf{r}_{pre}^n$ and $\tilde{\mathbf{r}}^n$ are the position vectors from the INS mechanization and pseudo-position, respectively; \mathbf{r}_{pre}^n is the position result at the last inertial sensor sampling time epoch by using the navigation algorithm, $\delta\mathbf{r}^n$ is the position error vector; and \mathbf{n}_1 is the measurement noises. This research utilizes zero-mean Gaussian white noises to model all measurement noises, which is similar to the majority of engineering applications. In practice, human motions commonly introduce some systematical errors or colored noises. Therefore, we enlarged the parameters for measurement noises for several times to make the algorithm robustness, as shown in [Section 3.5](#).

(b) Accelerometer measurement model

The measurement model is built by using accelerometer readings, instead of applying the accelerometers-derived roll and pitch angles. This choice is important for pedestrian applications with arbitrary phone displacements because it avoids the singularity

problem when the pitch angle reaches $\pm 90^\circ$. The accelerometer measurement model is given by [32]

$$\begin{aligned}\delta \mathbf{f}^n &= (\mathbf{I} - [\psi \times]) \mathbf{C}_b^n \mathbf{f}^b - \mathbf{f}^n + \mathbf{C}_b^n \mathbf{n}_2 \\ &= [\psi \times] \mathbf{g}^n + \mathbf{C}_b^n \mathbf{n}_2 = -[\mathbf{g}^n \times] \psi + \mathbf{C}_b^n \mathbf{n}_2\end{aligned}\quad (4)$$

where $\delta \mathbf{f}^n = \mathbf{C}_b^n \tilde{\mathbf{f}}^b - \mathbf{f}^n$, $\tilde{\mathbf{f}}^b$ is the accelerometer reading vector, $\mathbf{f}^n = -\mathbf{g}^n = [0 \ 0 \ -g]^T$ is the specific force in the n-frame, \mathbf{f}^b is the specific force in the b-frame, g is the local gravity value, ψ is the attitude error, \mathbf{I} is the identity matrix, and \mathbf{n}_2 is the noise. $[\mathbf{v} \times]$ denotes the skew-symmetric matrix of vector \mathbf{v} .

(c) Magnetometer measurement model

The main challenge for using magnetometer measurements indoors is the existence of frequent magnetic perturbations. A typical type of magnetic perturbation is that both the direction and strength of the LMF are changed, but the change is stable within a limited space (or time periods). The period during which the LMF is stable can be called as QSMF period, and can be detected by using the magnitude of magnetometer readings [32].

The proposed algorithm uses magnetometer measurements during QSMF periods. It is assumed that there is totally no idea about the LMF parameters. Instead, the proposed algorithm calibrates the LMF at the beginning of each QSMF period. The LMF vector during the k-th QSMF period is computed by [32]:

$$\mathbf{m}_k^n = (\mathbf{C}_n^b)^T \tilde{\mathbf{m}}_{k,1}^b \quad (5)$$

where $\tilde{\mathbf{m}}_{k,1}^b$ is the magnetometer reading at the beginning of the first epoch(s) of k-th QSMF period. The computed \mathbf{m}_k^n is then used as the reference during the k-th QSMF period.

The measurement model is built by using magnetometer readings directly. This strategy avoids the leveling step (i.e., using accelerometer readings to calculate the roll and pitch angles). Therefore, the measurement model (6) is independent from accelerometer measurements.

$$\delta \mathbf{m}^n = [\mathbf{m}^n \times] \psi + \mathbf{C}_b^n \mathbf{n}_3 \quad (6)$$

where $\delta \mathbf{m}^n = \mathbf{C}_b^n \tilde{\mathbf{m}}^b - \mathbf{m}^n$, $\tilde{\mathbf{m}}^b$ is the magnetometer reading vector, \mathbf{m}^n is the calibrated LMF vector, and \mathbf{n}_3 is the noise.

(d) Normal vectors of magnetometer and accelerometer measurements

The normal vector of two non-parallel vectors is orthogonal to both vectors [46]. The approach of using the norm vector of accelerometer and magnetometer measurement vectors has been developed for satellite TV antenna stabilization using an MEMS attitude and heading reference system (AHRS). The normal vector will suffer from less disturbances when either of these two vectors is perturbed [47]. When there are strong acceleration disturbances, the magnetometer measurement and the normal vector may be used. Contrarily, if the magnetometer measurement is perturbed, the accelerometer measurement and the normal vector may be used. When both accelerometer and magnetometer measurements are perturbed, all measurement updates will not be used in the attitude-determination EKF. The measurement model for the normal vector is

$$\delta \mathbf{l}^n = [\mathbf{l}^n \times] \psi + \mathbf{C}_b^n \mathbf{n}_4 \quad (7)$$

where $\delta \mathbf{l}^n = \mathbf{C}_b^n \tilde{\mathbf{l}}^b - \mathbf{l}^n$, $\mathbf{l}^n = \mathbf{f}^n \times \mathbf{m}^n$, $\mathbf{l}^b = \mathbf{f}^b \times \mathbf{m}^b$, and \mathbf{n}_4 is the noise.

The normal vector of accelerometer and magnetometer measurements is also used for the initial alignment (i.e., determination of initial attitude angles) of the INS mechanization. Denoting that $\tilde{\mathbf{f}}^b = \mathbf{C}_b^n \mathbf{f}^n$, $\tilde{\mathbf{m}}^b = \mathbf{C}_b^n \mathbf{m}^n$, and $\tilde{\mathbf{r}}^b = \mathbf{C}_b^n \mathbf{r}^n$, then

$$[\tilde{\mathbf{f}}^b \quad \tilde{\mathbf{m}}^b \quad \tilde{\mathbf{r}}^b]^T = [\mathbf{f}^n \quad \mathbf{m}^n \quad \mathbf{l}^n]^T \mathbf{C}_b^n \quad (8)$$

The initial direction cosine matrix from the b-frame to the n-frame can be computed by [48]

$$\mathbf{C}_b^n = \left([\mathbf{f}^n \quad \mathbf{m}^n \quad \mathbf{l}^n]^T \right)^{-1} [\tilde{\mathbf{f}}^b \quad \tilde{\mathbf{m}}^b \quad \tilde{\mathbf{r}}^b]^T \quad (9)$$

Eq. (10) is used to correct the attitude angles in the EKF.

$$\hat{\mathbf{C}}_b^n = (\mathbf{I} + [\psi \times]) \mathbf{C}_b^n \quad (10)$$

where $\hat{\mathbf{C}}_b^n$ is the corrected direction cosine matrix. The heading used for PDR is calculated by [49]

$$\hat{\psi} = \begin{cases} \tan_4^{-1}(c_{2,1}/c_{1,1}), & \text{if } -0.999 < c_{3,1} < 0.999 \\ \tan_4^{-1}([c_{2,3} - c_{1,2}]/[c_{1,3} + c_{2,2}]), & \text{if } c_{3,1} \leq -0.999 \\ \tan_4^{-1}([c_{2,3} + c_{1,2}]/[c_{1,3} - c_{2,2}]) + \pi, & \text{if } c_{3,1} \geq 0.999 \end{cases} \quad (11)$$

where $\tan_4^{-1}(\cdot)$ is a four-quadrant arctangent operator that can be implemented as the “atan2” function in many programming languages. $c_{i,j}$ is the element at the i-th row and j-th column of $\hat{\mathbf{C}}_b^n$. The heading $\hat{\psi}$ is fed into the position-tracking module that utilizes PDR to provide continuous position predictions.

2.2. PDR-based position-tracking EKF

2.2.1. Position-tracking EKF system model

The system model can be generated by using the PDR error model derived from (12). PDR is the relative means of determining of a new position (φ_k, λ_k) from a previous known position $(\varphi_{k-1}, \lambda_{k-1})$ using the latest heading and step length by:

$$\begin{bmatrix} \varphi_k \\ \lambda_k \end{bmatrix} = \begin{bmatrix} \varphi_{k-1} + s_k \cos \hat{\psi}_{k-1}/(R_m + h) \\ \lambda_{k-1} + s_k \sin \hat{\psi}_{k-1}/[(R_n + h)\cos \varphi_{k-1}] \end{bmatrix} \quad (12)$$

where $\hat{\psi}$ and s are heading and step length, and the subscript $k-1$ and k indicate the count of steps. R_m and R_n are the radii of curvature of meridian and curvature in the prime vertical of the Earth, and h is the height.

A PDR algorithm consists of three parts: step detection, step-length estimation, and heading estimation. Refer to [50] and [51] for details about step detection and step-length estimation, respectively. A linear step-length model that considers both walking frequency and acceleration variance is adopted:

$$s_k = \alpha \cdot f_k + \beta \cdot v_k + \gamma \quad (13)$$

$$f_k = 1/(t_k - t_{k-1}) \text{ and } v_k = \sum_{t=t_{k-1}}^{t_k} ((a_t - \bar{a}_k)^2 / N) \quad (14)$$

where f_k and v_k are walking frequency and acceleration variance, respectively; a is acceleration, \bar{a}_k and N are the mean value and the number of accelerations during the time period $[t_{k-1}, t_k]$; α , β , and γ are the parameters, which can be pre-learned during a pre-calibration stage.

2.2.2. Position-tracking EKF measurement model

The measurement model is built through the use of WiFi and MM results. The WiFi or MM measurement model is

$$\begin{bmatrix} \hat{\varphi}_{DR,k} - \hat{\varphi}_{WiFi \text{ or } MM,k} \\ \hat{\lambda}_{DR,k} - \hat{\lambda}_{WiFi \text{ or } MM,k} \end{bmatrix} = \begin{bmatrix} \delta \varphi + n_\varphi \\ \delta \lambda + n_\lambda \end{bmatrix} \quad (15)$$

where $\hat{\varphi}_{DR}$ and $\hat{\lambda}_{DR}$ are the latitude and longitude predicted by DR; $\hat{\varphi}_{WiFi \text{ or } MM}$ and $\hat{\lambda}_{WiFi \text{ or } MM}$ are the latitude and longitude from WiFi or MM; and n_φ and n_λ are the measurement noises. Technical details about WiFi fingerprinting and MM are provided in the next subsection.

2.3. WiFi fingerprinting and magnetic matching

WiFi fingerprinting and MM both consist of a training phase and a positioning phase, which are introduced separately.

2.3.1. Database training

A \langle location, RSS \rangle database and a \langle location, magnetic feature \rangle database are generated simultaneously in this phase. A walk-survey method is adopted. A surveyor is asked to hold the smartphone horizontally and walk along pre-designed survey trajectories that have landmarks (e.g., corners, intersections, and other preset landmarks), and record the time of passing every landmark. The coordinates of landmarks can be obtained from a digital indoor map, while the true orientation of links between adjacent landmarks can be calculated by using these coordinates. The landmark coordinates were obtained as follows: the indoor map was first overlapped onto the Google Earth; then, the landmark coordinates (i.e., latitude, longitude, and height) were obtained by putting the mouse pointer on the landmarks. Locations of RPs on the links between landmarks were calculated through interpolation using step points detected by accelerometers. To design the survey trajectory, in corridor areas, the middle lines of corridors were used; in lobby areas, the “S” shape was adopted to cover the area.

The accuracy of RP positions from walk-survey was evaluated by walking on a straight path with known length for 50 times, and comparing the results of dividing PDR-derived distances with the true path lengths. The RMS value of these results was 1.12. Thus, the maximum errors of RP positions may reach 10–20% of path length. To assure RP position accuracy, dense landmarks were used. The maximum distance between adjacent landmarks was set at 10 m. Thus, there are nearly 15 steps on each link. Considering the averaging mechanism on each link, the maximum value for the RP position errors was 0.25 m–0.50 m ($10 \text{ m} \cdot 10\% / \sqrt{15} = 0.25 \text{ m}$, $10 \text{ m} \cdot 20\% / \sqrt{15} = 0.50 \text{ m}$). Thus, RP locations obtained from walk-survey with dense landmarks were accurate enough for either building databases in the training phase, or generating reference trajectories for the evaluation of navigation results. To evaluate results, position errors were calculated by using the following method: assuming the positioning results at time k is $[\varphi_k \lambda_k]$ and the position of the corresponding point on the reference trajectory is $[\varphi_{r,k} \lambda_{r,k}]$, the position error at time k is

$$D_k = \sqrt{[(\varphi_k - \varphi_{r,k})(R_m + h)]^2 + [(\lambda_k - \lambda_{r,k})(R_n + h)\cos(\varphi_{r,k})]^2} \quad (16)$$

Android smartphones commonly have low WiFi RSS update rates (e.g., 0.3–0.5 Hz for the tested Samsung Galaxy S4 and Xiaomi 4 smartphones, as collected by the class “WifiManager”). Thus, when a new RSS comes, the last step point is recorded as an RP. The WiFi fingerprint at the i -th RP is recorded as

$$\mathbf{FW}_i = \{\mathbf{pos}_i, (mac_{i,1}, RSS_{i,1}), (mac_{i,2}, RSS_{i,2}), \dots, (mac_{i,m_i}, RSS_{i,m_i})\} \quad (17)$$

where \mathbf{pos}_i is the coordinate of RP_i , $mac_{i,j}$ and $RSS_{i,j}$ are the media access control (MAC) address and RSS of the j -th AP at RP_i , and m_i is the number of available APs at RP_i .

Magnetometers have high sampling rates. Therefore, all step points are stored as MM RPs. Additionally, assuming the device moves with a constant speed between adjacent step points, a set of RPs can be obtained between these step points through interpolation. The magnetic-intensity fingerprint at the k -th RP, RP_k , is recorded as

$$\mathbf{FM}_k = \{\mathbf{pos}_k, B_k\} \quad (18)$$

where \mathbf{pos}_k and $B_k = \sqrt{B_{x,k}^2 + B_{y,k}^2 + B_{z,k}^2}$ represent the coordinates and magnetic intensity at RP_k , respectively; $B_{x,k}$, $B_{y,k}$, and $B_{z,k}$ are the x-, y-, and z-axis magnetometer readings.

Two methods are used to increase the magnetic fingerprint dimension: (1) by using roll and pitch angles detected by accelerometers, the magnetic fingerprint at RP_k can be changed to

$$\mathbf{FM}_k = \{\mathbf{pos}_k, B_{h,k}, B_{v,k}\} \quad (19)$$

where $B_{v,k} = -\sin \theta_k \cdot B_{x,k} + \sin \phi_k \cdot B_{y,k} + \cos \phi_k \cos \theta_k \cdot B_{z,k}$ and $B_{h,k} = \sqrt{B_k^2 - B_{v,k}^2}$ are the vertical and horizontal magnetic intensities, respectively, ϕ_k and θ_k are the roll and pitch angles. (2) magnetic-intensity-profile fingerprints are used. The magnetic-intensity-profile fingerprint at RP_k is

$$\mathbf{FP}_k = \{\mathbf{pos}_k, \mathbf{m}_{h,k}, \mathbf{m}_{v,k}\} \quad (20)$$

where $\mathbf{m}_{h,k} = [B_{h,k}, B_{h,k-1}, \dots, B_{h,k-N}]$ and $\mathbf{m}_{v,k} = [B_{v,k}, B_{v,k-1}, \dots, B_{v,k-N}]$ are the horizontal and vertical magnetic-intensity profiles, respectively. $N = (n+1) \cdot T$, where T is the number of steps used to generate a magnetic-intensity profile and n is the number of interpolation points between two step points. The final magnetic fingerprint at RP_k is

$$\mathbf{FG}_k = \{\mathbf{pos}_k, \mathbf{m}_{h,k}, \mathbf{r}_{h,k}, \mathbf{m}_{v,k}, \mathbf{r}_{v,k}\} \quad (21)$$

where $\mathbf{r}_{h,k} = [B_{h,k} - B_{h,k}, B_{h,k-1} - B_{h,k}, \dots, B_{h,k-N} - B_{h,k}]$ and $\mathbf{r}_{v,k} = [B_{v,k} - B_{v,k}, B_{v,k-1} - B_{v,k}, \dots, B_{v,k-N} - B_{v,k}]$ are defined as the horizontal and vertical magnetic-gradient profiles. The position of the end point of a profile is used as \mathbf{pos}_k .

2.3.2. Positioning

WiFi fingerprinting is based on point-by-point matching, while MM is a profile-matching technique. The WiFi fingerprinting and MM algorithms are described separately.

(a) WiFi fingerprinting

The basic idea of WiFi fingerprinting is calculating the difference between the measured fingerprint and candidate fingerprints in database to find the optimal match. To compare the measured vector with the i -th database fingerprint, two vectors, \mathbf{S} and \mathbf{M}_i , are used to represent the RSS values at the measured point and the i -th RP, respectively. Both \mathbf{S} and \mathbf{M}_i consist of N RSS values that correspond to the union of the available APs at both the measured point and the i -th RP. The RSS from the N APs follow the same sequence in \mathbf{S} and \mathbf{M}_i . The RSS for an unavailable AP is set at -100 dBm. For example, if the fingerprints at the measured point and the i -th RP are $\{\mathbf{pos}_S, (mac_{AP_1}, RSS_{AP_1}), (mac_{AP_2}, RSS_{AP_2})\}$ and $\{\mathbf{pos}_{M_i}, (mac_{AP_3}, RSS_{AP_3}), (mac_{AP_4}, RSS_{AP_4})\}$, \mathbf{S} and \mathbf{M}_i are constructed as $\mathbf{S} = [RSS_{AP_1}, RSS_{AP_2}, -100 \text{ dBm}, -100 \text{ dBm}]$ and $\mathbf{M}_i = [-100 \text{ dBm}, -100 \text{ dBm}, RSS_{AP_3}, RSS_{AP_4}]$, respectively. The optimal match between \mathbf{S} and \mathbf{M}_i can be indicated by the smallest Euclidean distance d_i :

$$d_i = \|\mathbf{S} - \mathbf{M}_i\|_p = \left(\sum_{j=1}^N |\mathbf{S}_j - \mathbf{M}_{i,j}|^p \right)^{1/p} \quad (22)$$

where $p = 2$ in this research. \mathbf{S}_j and $\mathbf{M}_{i,j}$ are the j -th elements in \mathbf{S} and \mathbf{M}_i , respectively.

To enhance reliability, the k-NN method [52] is used to provide WiFi fingerprinting results through calculating the weighted averaging of positions of the k selected RPs that have the smallest Euclidean distances. The equation for weighted averaging is

$$\hat{\mathbf{r}} = \sum_{i=1}^k ((c_i/C) \mathbf{r}_i) \quad (23)$$

where $c_i = 1/d_i$, $C = \sum_{i=1}^k c_i$, \mathbf{r}_i is the position of the i -th selected RP, and $\hat{\mathbf{r}}$ is the estimated position. A special case is that when a certain d_i is zero, the estimation of \mathbf{r}_i can be taken as $\hat{\mathbf{r}}$.

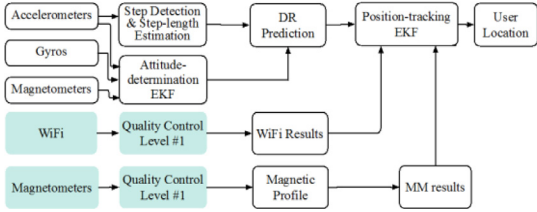


Fig. 1. Structure #0 for DR/WiFi/MM integration.

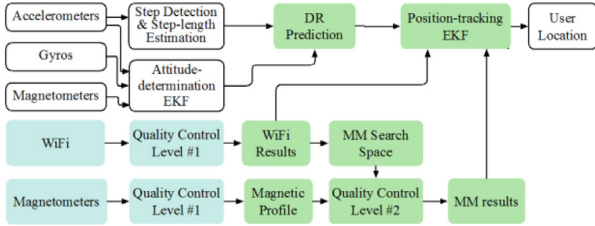


Fig. 2. Structure #1 for DR/WiFi/MM integration.

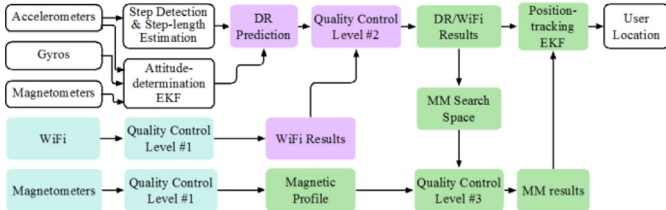


Fig. 3. Structure #2 for DR/WiFi/MM integration.

(b) Magnetic matching

If a measured magnetic profile has the same length as those in the database, the MM algorithm is same as [22], where \mathbf{S} is the measured magnetic profile, \mathbf{M}_i is the i -th candidate database profile, and N is the length of magnetic profile. However, real-time step-length estimation is challenging, which makes it difficult to obtain an accurate profile length. Thus, DTW [53] is used. The technique in DTW is to compress or stretch the time axes of both (or one) sequences to achieve a better alignment between two sequences, $\mathbf{S}(i)$, $i = 1, 2, \dots, A$ and $\mathbf{M}(j)$, $j = 1, 2, \dots, B$, that have different lengths. Algorithm 1 illustrates the process of DTW. Refer to [37] for details about MM, and [54] for MM using DTW.

To reduce the impact of MM mismatches, the k-NN method is also introduced to obtain MM results by calculating the weighted average of positions at the end points of the k selected candidate profiles that have the smallest differences to the measured one.

2.4. Improved DR/WiFi/MM integration structures

Three DR/WiFi/MM integration structures (i.e., Structures #0, #1, and #2) are evaluated. These structures use the same DR algorithm to build the EKF system model, and adopt different strategies on using WiFi and MM results as updates. In Structure #0, these results are directly used, which is similar to most of previous works. In Structure #1, WiFi results are used to limit the MM search space and obtain MM (WiFi aided) results. Afterwards, both WiFi and MM (WiFi aided) results are integrated with DR. Finally, Structure #2 integrates DR with WiFi, and uses DR/WiFi results to limit the MM search space. The diagram of these structures are illustrated in Figs. 1–3, respectively. In the attitude-determination EKF, the inputs are readings from gyros, accelerometers and magnetometers, and apriori information of pseudo-observations; the output is the heading angle. In the position-tracking EKF, the inputs are the DR position predictions and the WiFi and MM posi-

tion updates, while the output is the user location. An essential improvement in Structure #2 is the use of QC methods, which are introduced in Sections 2.4.1–2.4.3.

Structure #2 is designed based on the advantages and disadvantages of DR, WiFi, and MM:

- DR is a self-contained technique that has a potential to be the backbone of a continuous and reliable navigation solution. However, low-cost sensor-based DR suffers from issues such as initialization errors, sensors errors, and the misalignment angle between the smartphone and the human body. Thus, DR can be used as an aiding information to improve the reliability of the other techniques. DR is used for three times in Structure #2, specifically, for the QC of WiFi and MM, and for the generation of the EKF system model. The former two are implemented to obtain reliable WiFi and MM results while the third is to provide position predictions.
- WiFi is essential to provide the initial position, and has a merit of a low mismatch rate, which makes it suitable for aiding both DR and MM. However, WiFi positioning methods suffer from RSS fluctuations in indoor environments. Thus, Structure #2 further uses the integration of DR/WiFi to replace WiFi and determine the MM search space.
- MM can provide results with small fluctuations, but suffers from a high mismatch rate. Therefore, MM is suitable to provide position updates at the final step, with a precondition that the MM mismatches have been removed.

A three-level QC mechanism is designed in Structure #2 based on the interaction between different techniques, as indicated in Fig. 3. The explanation of these levels are provided below.

2.4.1. Level #1: QC on wifi and MM measurements

The purpose of this level is to filter out blunders or unreliable measurements of WiFi and MM. Because DR is self-contained and relative robust, this level is mainly on WiFi and MM. Several criteria are applied to detect WiFi blunders, such as (a) the number of observed APs must be over the threshold Th_{AP} ; (b) the useful WiFi RSS should be strong enough than the threshold Th_{RSS} ; and (c) the Euclidean distance should be less than the threshold Th_{d1} .

MM is conducted only when the measured magnetic fingerprint has a distinct magnetic feature. The change range (i.e., difference between the maximum and minimum values) and the standard deviation value of magnetometer measurements during a certain time period are calculated to detect the fingerprints with indistinct features. Specifically, the fingerprint T passes the QC test when $Diff_T > th_{m1}$ and $Std_T > th_{m2}$, where $Diff_T$ and Std_T are the range and standard deviation of the magnetic intensities at T , th_{m1} and th_{m2} are the corresponding threshold values.

2.4.2. Level #2: QC on DR/WiFi fusion

The weight of WiFi positioning results can be set automatically through the investigation of the EKF innovation sequence [55,56]. In this paper, a practical threshold-based method is used: the WiFi position uncertainties at time k are set based on the distance d_k between the new WiFi position and the historical positioning solutions: when $d_k \leq th_{WiFi1}$, the uncertainties are set at σ_{WiFi} ; when $th_{WiFi1} < d_k \leq th_{WiFi2}$, the uncertainties are set at $s_{WiFi}\sigma_{WiFi}$, where s_{WiFi} is a scalar; finally, when $d_k > th_{WiFi2}$, the uncertainties are set at a large number $\sigma_{WiFiMax}$, which indicates the new WiFi position will not contribute to the solution. th_{WiFi1} and th_{WiFi2} are empirical threshold values determined by preliminary tests in the same area.

2.4.3. Level #3: QC on mM

The basic idea of this level is utilizing DR/WiFi positioning results to limit the MM search space. The search space can be limited to an ellipse shown in Fig. 4.

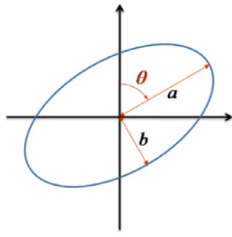


Fig. 4. Sample ellipse-based MM search space.

The center of the ellipse is located at the DR/WiFi result, while the major semi-axis, minor semi-axis, and the azimuth (i.e., the angle measured clockwise from the north) are obtained through the use of the position covariance matrix from the EKF, that is

$$\mathbf{P} = \begin{bmatrix} \sigma_N^2 & \sigma_{NE} \\ \sigma_{EN} & \sigma_E^2 \end{bmatrix} \quad (24)$$

where σ_N^2 and σ_E^2 are the north and east position variances; σ_{NE} is the covariance between north and east; and σ_{EN} is that between east and north. Based on the theory of confidence ellipse for measurement [57], the major semi-axis of the ellipse is

$$a = s_e \cdot \sqrt{0.5(\sigma_N^2 + \sigma_E^2) + \sqrt{0.25(\sigma_E^2 - \sigma_N^2)^2 + \sigma_{NE}^2}} \quad (25)$$

and the minor semi-axis is

$$b = s_e \cdot \sqrt{0.5(\sigma_N^2 + \sigma_E^2) - \sqrt{0.25(\sigma_E^2 - \sigma_N^2)^2 + \sigma_{NE}^2}} \quad (26)$$

The azimuth of the major semi-axis is

$$\theta = 0.5 \tan^{-1}(2\sigma_{NE}/(\sigma_E^2 - \sigma_N^2)) \quad (27)$$

At the beginning of navigation, the initialization of navigation is not accurate due to the lack of apriori information; thus, the value of the scale factor s_e is set at the large number (e.g., 30) to avoid removing correct MM results. Afterwards, the area of the ellipse becomes smaller gradually as the navigation solution becomes more accurate. Finally, the value of s_e is fixed at 3. Besides ellipses, other shapes such as circles or squares can be used to define the search space.

3. Tests description

3.1. Test platform

The experiment platform can be any Android smartphone equipped with gyros, accelerometers, magnetometers, and a WiFi receiver. The sensor data was collected through the Java Native Interface (JNI) mechanism, while the WiFi data was collected through the class “WiFiManager”. The sample rate of sensors was set at 20 Hz, while the WiFi update rate was 0.3–0.5 Hz.

Two smartphones were used: a Samsung Galaxy S4 and a Xiaomi 4. **Table 1** illustrates the specifications of the inertial sensors in these smartphones.

It is clear that low-cost MEMS inertial sensors may suffer from significant run-to-run biases and thermal drifts. We simply implement a quick hand calibration for each smartphone for once by following the research [45]. Such calibration is affordable for consumer portable devices as it is easy to be implemented without any equipment. The run-to-run biases and thermal drifts were not calibrated specifically.

3.2. Tested motion conditions

Compared with most of the previous research that focuses on the handheld condition, this research aims to provide a reliable so-

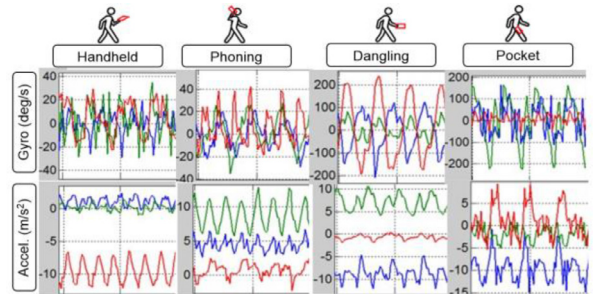


Fig. 5. Gyro and accelerometer signals under tested motion conditions.



Fig. 6. Indoor test environment at Building #1 (typical office environment).

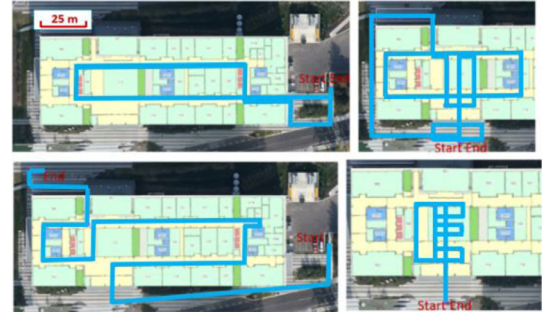


Fig. 7. Trajectories for generating WiFi and MM databases at Building #1.

lution when the user changes the smartphone motion conditions. Since it is difficult for low-cost sensors themselves to detect the accurate misalignment angle, it is important to use information from other sources to reduce its impact.

The tested motion conditions included those with typical phone locations, including handheld, phoning, dangling, and pocketed. **Fig. 5** shows these motions and typical sensor readings. The algorithm is required to provide a consistent reliable solution under different motion conditions.

3.3. Test areas and database generation

Two areas were selected at the University of Calgary, one on the main floor of Building #1, the other on the lower main floor of Building #2. Building #1 represents a typical office environment, while Building #2 is a public area which is mainly used for walking. In Building #1, the average number of RSS on each RP was over 15, and the change of magnetic intensity reached 0.4 Gauss. The size of tested area at Building #1 is around $120 \times 40 \text{ m}^2$. There is a main corridor which is 3 m wide, and a lobby which is $30 \times 30 \text{ m}^2$. **Fig. 6** shows the environment inside Building #1, and **Fig. 7** illustrates the indoor map and trajectories used for generating databases. The test area and trajectories for database generation is same to the previous research [60].

The database training process was efficient by using the walk-survey approach described in **Section 2.2.1**: each trajectory lasted for approximate 6 minutes, and the whole area was surveyed within half an hour. As the WiFi update rate was 0.3–0.5 Hz, the distance between adjacent WiFi RPs on one trajectory was

Algorithm 1
Dynamic Time Warping.

Given: One-dimensional series \mathbf{S} and \mathbf{M} with length m and n , respectively.

1. **Let** \mathbf{d} be the matrix that contains the distance among pairs of values in \mathbf{S} and \mathbf{M} ;
2. **For** $i = 0$ to $m - 1$
3. **For** $j = 0$ to $n - 1$
4. $\mathbf{d}(i, j) = (\mathbf{S}(i) - \mathbf{M}(j))^2$;
5. **End for**
6. **End for**
7. **Let** \mathbf{D} be the matrix that contains the DTW distance among pairs of values in \mathbf{S} and \mathbf{M} ;
8. $\mathbf{D}(0, 0) = \mathbf{d}(0, 0)$;
9. **For** $i = 1$ to $m - 1$
10. $\mathbf{D}(i, 0) = \mathbf{d}(i, 0) + \mathbf{D}(i - 1, 0)$;
11. **For** $j = 1$ to $n - 1$
12. $\mathbf{D}(0, j) = \mathbf{d}(0, j) + \mathbf{D}(0, j - 1)$;
13. $\mathbf{D}(i, j) = \mathbf{d}(i, j) + \dots$
 $\min(\mathbf{D}(i - 1, j), \mathbf{D}(i - 1, j - 1), \mathbf{D}(i, j - 1))$
14. **End for**
15. **End for**

Obtain: the DTW distance matrix \mathbf{D} .

Table 1
Specifications of inertial sensors in tested smartphones.

	IMPU-6500 [58] (InvenSense)	LSM9DSO [59] (ST Microelectronics)
Gyro	At 25 °C: ±5 deg/s	At 25 °C: ±10 deg/s
Biases	Thermal drifts: ±0.24 deg/s/ °C (-40 to +85 °C)	Thermal drifts: ± 0.05 deg/s/ °C (-40 to +85 °C)
ARW	0.6 deg/h ^{1/2}	Unknown
Accel.	At 25 °C: ± 60 mg	At 25 °C: ± 60 mg
Biases	Thermal drifts: ± 0.64 mg/ °C (-40 to +85 °C)	Thermal drifts: ± 0.5 mg/ °C (-40 to +85 °C)
VRW	0.18 m/s/h ^{1/2}	Unknown

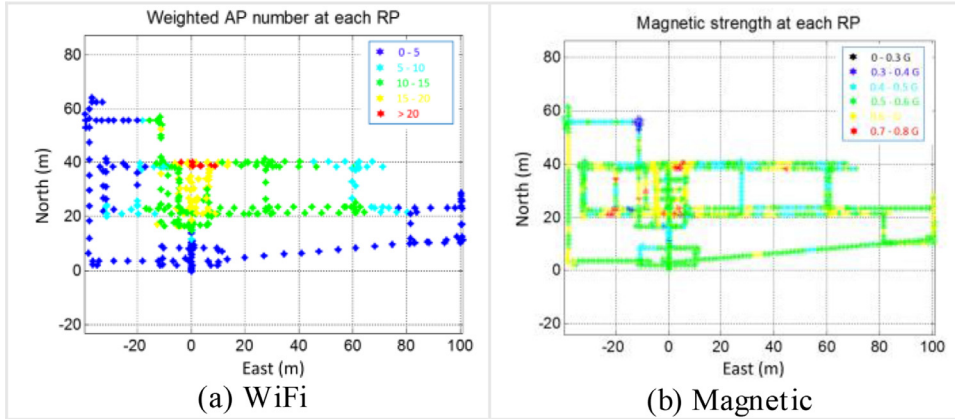


Fig. 8. Distribution of WiFi signal and magnetic intensity at Building #1.

nearly 3 m, and there was only one WiFi measurement on each RP. There were 287 WiFi RPs and 27,863 MM RPs in the database at Building #1. During the database training process, there were over thirty people walking around, which might impact the performance of databases. This research does not make efforts to enhance databases because it is not always affordable to obtain a high-accuracy database in a public area; meanwhile, the changes of databases over time may degrade the contribution of a high-accuracy database. The low performance of databases poses more challenges, and thus can better evaluate the algorithm.

Meanwhile, we directly used existing WiFi APs in tested areas. Colors in Figs. 8(a) and (b) indicate the weighted AP number and the magnetic intensity in the databases, respectively. The magnetic intensity varied between 0.3 and 0.8 Gauss indoors. The weighted AP number at RP_i was $WAP_i = \sum_{j=1}^{n_i} a_{i,j}$, where n_i is the number of RSS, $a_{i,j}$ is determined according to $RSS_{i,j}$ (i.e., the RSS of AP_j at RP_i): if $RSS_{i,j} > -60$ dBm, $a_{i,j} = 1$; if -70 dBm $< RSS_{i,j} < -60$ dBm, $a_{i,j} = 0.75$; if -85 dBm $< RSS_{i,j} < -70$ dBm, $a_{i,j} = 0.25$; if $RSS_{i,j} < -85$ dBm, $a_{i,j} = 0$.



Fig. 9. Indoor test environment at Building #2 (public area for walking).

There are less WiFi APs and magnetic interferences at Building #2. Fig. 9 shows the indoor environment, which was nearly 140×60 m². Figs. 10 (a) and (b) show the RSS and magnetic distributions on the test trajectory, respectively. There were 188 WiFi RPs and 10,494 MM RPs in the database. The average number of RSS was approximately seven at Building #2, and the change of magnetic intensity was below 0.25 Gauss.

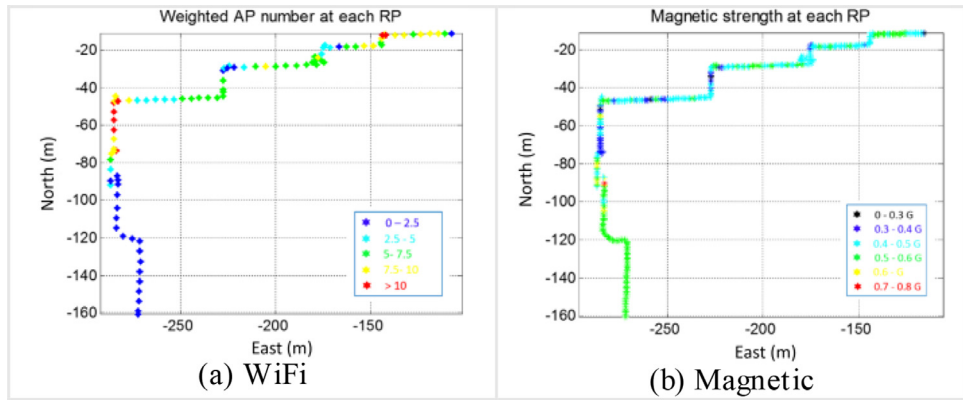


Fig. 10. Distribution of WiFi signal and magnetic intensity at Building #2.



Fig. 11. Test trajectories used in Group #1, #2, and #3.

Table 2
Conditions of three test groups.

Test Group	#1	#2	#3
Initialized before tests	Yes	No	No
Changed motion conditions during tests?	No	Yes	No
Time period between pre-survey and positioning	1 day	4 months	1 day
Building for test	#1	#1	#2

3.4. Test arrangements

Three groups of tests were conducted to evaluate different DR/WiFi/MM integration structures. These test groups were set based on four factors: the initialization of navigation, the tested motion conditions, the timeliness of databases, and the differences of environments, as illustrated in Table 2.

Specifically, Group #1 was similar to most of the previous experiments on DR, which assumed that the initial position and heading was known. This assumption is valid when navigation is an “always-on” application that runs in the background of the smartphone operation system because initialization can be completed when GNSS is available. In Groups #2 and #3, the user started navigation indoors, and WiFi and magnetometers were utilized to initialize position and heading, respectively. We set the weight of initial position and heading at small values, and updated them during navigation. Therefore, it is key to investigate how to utilize the information from multiple sensors in a robust way.

Group #2 was used to evaluate the long-term navigation performances as well as the repeatability of the solution. Two types of tests were conducted. In type #1, the smartphone was handheld horizontally during the whole test, while in type #2, the user switched among different motion conditions. Type #2 is much more challenging because changes of motions may introduce a misalignment angle. The occurrence of the misalignment angle may not be an issue outdoors as GNSS can provide frequent and

reliable position updates; however, in indoor area, GNSS is not available, and both WiFi and MM may not be reliable because they are dependency on environments.

Group #3 was used to evaluate the navigation performances in environments that had different WiFi and magnetic distributions.

The test trajectories used in three test groups are illustrated in Fig. 11. The test trajectories were different from the training ones. Also, the walk directions on the majority of the main corridors were opposite from those on the training trajectories.

3.5. Setting of the EKF parameters

Setting of EKF parameters is key to a robust navigation solution. Indoor environments are complex and unpredictable. Thus, although various tests had different motion conditions and environments, we used the same set of EKF parameters to evaluate the consistency and robustness of the algorithm.

The EKF parameters include the initial state vector (i.e., $\mathbf{x}_{0,INS} = [\delta\mathbf{r} \ \delta\mathbf{v} \ \delta\psi \ \mathbf{b}_g \ \mathbf{b}_a]$ for the attitude-determination EKF, and $\mathbf{x}_{0,PDR} = [\delta\varphi \ \delta\lambda \ \delta\psi \ \delta s]$ for the position-tracking EKF) and the corresponding initial values of INS (i.e., the initial position, velocity and attitude, $\hat{\mathbf{r}}(t_0)$, $\hat{\mathbf{v}}(t_0)$, $\hat{\mathbf{att}}(t_0)$) and PDR (i.e., the initial latitude, longitude, heading, and step length, $\hat{\varphi}(t_0)$, $\hat{\lambda}(t_0)$, $\hat{\psi}(t_0)$, and $\hat{s}(t_0)$), the corresponding initial covariance matrices of the state vector ($\mathbf{P}_{0,INS}$ for INS and $\mathbf{P}_{0,PDR}$ for PDR), the covariance matrices of system noises (\mathbf{Q}_{INS} for INS and \mathbf{Q}_{PDR} for PDR) and the covariance matrices of measurement noises (\mathbf{R}_{pseudo} , \mathbf{R}_{accel} , \mathbf{R}_{mag} , and \mathbf{R}_{norm} for pseudo-observation, accelerometer measurements, and magnetometer measurements, and their normal vectors, respectively; and \mathbf{R}_{WiFi} and \mathbf{R}_{MM} for WiFi and MM positions, respectively).

In the attitude-determination EKF, the parameters were set at

$$\mathbf{x}_{0,INS} = \mathbf{0} \text{ (i.e., } \delta\mathbf{r} = \delta\mathbf{v} = \delta\psi = \mathbf{b}_g = \mathbf{b}_a = \mathbf{0});$$

$$\hat{\mathbf{r}}(t_0) = \mathbf{r}_{WiFi0}; \hat{\mathbf{v}}(t_0) = \mathbf{0}; \hat{\mathbf{att}}(t_0) = [\text{roll}_0 \ \text{pitch}_0 \ \psi_{mag0}]^T;$$

$$\mathbf{P}_{0,INS} = \text{diag}([\mathbf{var}(\mathbf{r}_0) \quad \mathbf{var}(\mathbf{v}_0) \quad \mathbf{var}(\psi_0) \quad \mathbf{var}(\mathbf{b}_{g0}) \quad \mathbf{var}(\mathbf{b}_{a0})]);$$

$$\mathbf{Q}_{INS} = \text{diag}([\mathbf{0} \quad \mathbf{VRW}^2 \quad \mathbf{ARW}^2 \quad \mathbf{q}_g^2 \quad \mathbf{q}_a^2]);$$

$$\mathbf{R}_{pseudo} = \text{diag}(\mathbf{var}(\mathbf{r}_{pseudo})), \mathbf{R}_{accel} = \text{diag}(\mathbf{var}(\mathbf{a}_{accel}))$$

$$\mathbf{R}_{mag} = \text{diag}(\mathbf{var}(\mathbf{m}_{mag})); \text{ and } \mathbf{R}_{norm} = \text{diag}(\mathbf{var}(\mathbf{m}_{norm}))$$

where $\mathbf{r}_{WiFi0} = [\varphi_{WiFi0} \quad \lambda_{WiFi0} \quad h_{WiFi0}]$ was comprised of the initial latitude and longitude from WiFi and the initial height (set at a random constant in this research), $roll_0$ and $pitch_0$ were the initial roll and pitch angles determined by the averaged accelerometer outputs in the first second. ψ_{mag0} was the heading calculated from magnetometer measurements and the IGRF model [22]. The values of $\mathbf{var}(\mathbf{r}_0)$, $\mathbf{var}(\mathbf{v}_0)$, $\mathbf{var}(\psi_0)$, $\mathbf{var}(\mathbf{b}_{g0})$, and $\mathbf{var}(\mathbf{b}_{a0})$ were set at $([30; 30; 10] \text{ m})^2$, $([0.1; 0.1; 0.1] \text{ m/s})^2$, $([10; 10; 90] \text{ deg})^2$, $([1; 1; 1] \text{ deg/s})^2$, and $([10; 10; 10] \text{ mg})^2$, respectively. The uncertainties of initial position and heading were large because the initial position and heading were not reliable. The **ARW**, **VRW**, \mathbf{q}_g , and \mathbf{q}_a values were obtained from sensor datasheets. The values of $\mathbf{var}(\mathbf{r}_{pseudo})$, $\mathbf{var}(\mathbf{a}_{accel})$, $\mathbf{var}(\mathbf{m}_{mag})$ and $\mathbf{var}(\mathbf{m}_{norm})$ were set at $([0.1; 0.1; 0.1] \text{ m})^2$, $([10; 10; 10] \text{ m/s})^2$, $([0.1; 0.1; 0.1] \text{ Gauss})^2$, and the product of $([10; 10; 10] \text{ m/s})$ and $([0.1; 0.1; 0.1] \text{ Gauss})$, respectively. These values were many times larger than the actual values of corresponding parameters because actual motion may introduce systematical errors that break the white noise assumption of EKF.

In the position-tracking EKF, the parameters were set at

$$\mathbf{x}_{0,PDR} = \mathbf{0} (\text{i.e., } \delta\varphi = \delta\lambda = \delta\psi = \delta s = 0);$$

$$\hat{\varphi}(t_0) = \varphi_{WiFi0}, \hat{\lambda}(t_0) = \lambda_{WiFi0}, \hat{\psi}(t_0) = \psi_{mag0}, \hat{s}(t_0) = s_0;$$

$$\mathbf{P}_{0,PDR} = \text{diag}([\mathbf{var}(\varphi_0) \quad \mathbf{var}(\lambda_0) \quad \mathbf{var}(\psi_0) \quad \mathbf{var}(s_0)]);$$

$$\mathbf{Q}_{PDR} = \text{diag}([q_\psi^2 \quad q_s^2 \quad 0 \quad 0]);$$

$$\mathbf{R}_{WiFi} = \text{diag}(\mathbf{var}(\mathbf{r}_{WiFi})); \mathbf{R}_{MM} = \text{diag}(\mathbf{var}(\mathbf{r}_{MM}))$$

where the values of $\mathbf{var}(\varphi_0)$, $\mathbf{var}(\lambda_0)$, and $\mathbf{var}(s_0)$ were set at $(30 \text{ m})^2$, $(30 \text{ m})^2$, and $(0.1 \text{ m})^2$, respectively. The values of q_ψ and q_s were set at 2 deg and 0.05 m. The value of s_0 was set at 0.65 m. The values of $\mathbf{var}(\mathbf{r}_{WiFi})$ and $\mathbf{var}(\mathbf{r}_{MM})$ are set in the QC mechanism.

For WiFi, the values of Th_{AP} (i.e., threshold for the minimum number of observed APs), Th_{RSS} (i.e., threshold for RSS), Th_{d1} (i.e., threshold for Euclidean distance) were set at 4, -85 dBm, and $10 \cdot \sqrt{n_{AP}}$ dBm, respectively, where n_{AP} is the number of RSS. The value of σ_{WiFi} (i.e., WiFi position uncertainty) was set at 5 m, and

the value of s_{WiFi} was set at d_k/σ_{WiFi} , where d_k was the distance between the new WiFi position and the previous position solution. The values of th_{WiFi1} and th_{WiFi2} were set at one time and three times of σ_{WiFi} .

For MM, the values of th_{m1} and th_{m2} were set at 0.1 Guass and 0.05 Guass, respectively. The number of steps used for MM, T , was set at 10: the MM process began after the user had walked for 10 steps; afterwards, the magnetic fingerprints within the latest 10 steps were used. The radii of the MM search spaces determined by WiFi and DR/WiFi results were set at 15 m and 10 m, respectively. The number of interpolation numbers between two step points, n , was set at 8. The k in k-NN were set at 3 for both WiFi and MM.

4. Results and discussion

For each test group, data from sensors and WiFi was processed by using nine strategies: DR, WiFi, DR/WiFi, MM #0 (i.e., original MM with QC #1), MM #1 (i.e., MM with QC #1 and aided by WiFi), MM #2 (i.e., MM with QC #1 and aided by DR/WiFi), DR/WiFi/MM #0 (i.e., Structure #0), DR/WiFi/MM #1 (i.e., Structure #1), and DR/WiFi/MM #2 (i.e., Structure #2). Both position errors and mismatch rates were calculated. The reference positions were obtained by using the walk-survey method described in Section 2.2.1. The mismatch rate was calculated by

$$\text{Mismatch rate} = (N_{i,ms}/N_{i,all}) \times 100 \% \quad (28)$$

where $N_{i,ms}$ represents the number of result points that had position errors of over 15 m, and $N_{i,all}$ is the total number of results points on this navigation trajectory.

4.1. Results of test group #1

Two testers walked along the trajectory in Fig. 11(a) for four times with four smartphone motions. Figs. 12 illustrates the pocketed results as examples. In (a), (c), and (g) - (i), the results were continuous and shown by lines; in (b) and (d) - (f), the marks illustrated the results while the lines indicated their sequences.

Figs. 12 demonstrates the following outcomes:

- DR solutions were continuous and had a similar shape as the true trajectory, but suffered from increasing position errors.
- WiFi results had long-term accuracy but had low sampling rates and suffered from fluctuations, especially in the lobby area. When integrated with DR, the results became continuous and smoother, but still had significant errors in this pocketed test.
- MM #0 results had small fluctuations but were vulnerable to mismatches. The majority of mismatches were eliminated in MM #1. More mismatches were removed in MM #2.
- Both DR/WiFi/MM #1 and #2 results were accurate, while the DR/WiFi/MM #0 result diverged on several occasions.

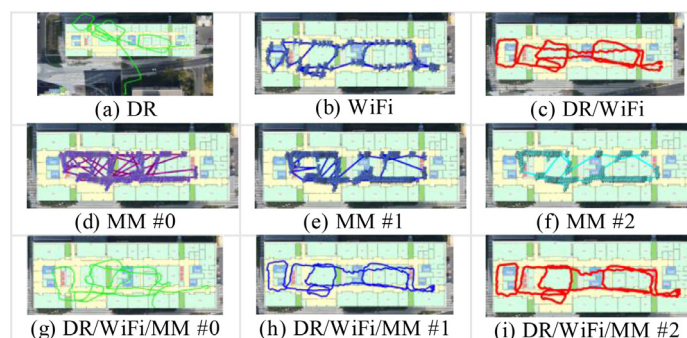


Fig. 12. Position results when using different strategies (Pocketed).

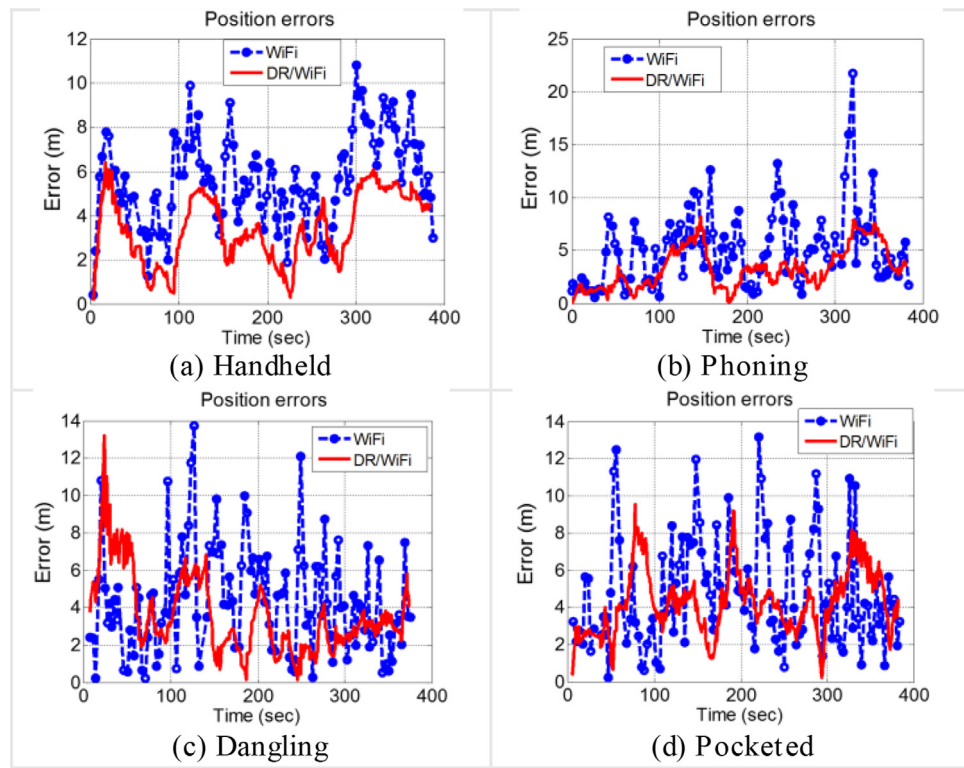


Fig. 13. Position errors of WiFi and DR/WiFi (Group #1).

Position errors were calculated to evaluate the navigation performance. Because one advantage of the proposed Structure #2 over Structure #1 is using DR/WiFi to replace WiFi, we compared the results from the following techniques or combinations: (i) WiFi and DR/WiFi; (ii) MM #0, #1, and #2; and (iii) DR/WiFi/MM #0, #1, and #2. The position errors of (i), (ii), and (iii) are demonstrated in Figs. 13–15, respectively.

Fig. 13 illustrates the following results:

- When integrated with DR, the majority of WiFi jump points (over 10 m) were removed, and the solutions became smooth.
- DR/WiFi results were more accurate under handheld and phoning because DR results were better under these motions.

Fig. 14 shows that

- The maximum error dropped from over 80 m for MM #0 to approximately 20 m for MM #1.
- The majority of MM #2 errors were below 10 m. The maximum MM #2 error occurred during 150 to 200 seconds of dangling. There were a series of MM mismatches; part of these mismatches were detected by DR/WiFi while others were not.
- MM #2 results were discontinuous but accurate. Thus, they can be used as reliable updates for the position-tracking EKF.

Fig. 15 indicates the following outcomes:

- The significant position errors were mitigated when either DR/WiFi/MM #1 or #2 was used. This outcome indicates the effectiveness of QC.
- DR/WiFi/MM #2 provided the most accurate results at most of the time.

To summarize, Fig. 16 provides the cumulative distribution function (CDF) curves of position errors, and Table 3 illustrates the statistical values of errors (i.e., RMS and the error within which the probability is 80%) and the mismatch rate.

Figs. 15 and 16 and Table 3 demonstrate that

- WiFi fingerprinting provided a better performance (RMS 5.7 m) than DR (RMS 17.1 m) and MM (RMS 20.0 m), as DR and MM suffered from drifts and mismatches, respectively.
- When integrated with DR, the RMS of WiFi errors were reduced to 4.0 m. Also, when aided by WiFi, the RMS of MM errors decreased to 5.1 m.
- When using MM #0 as position updates besides DR and WiFi, the reliability was degraded (the mismatch rate reached 9.7%). However, the mismatch rate was reduced to zeroes in both DR/WiFi/MM #1 and #2 results.
- The RMS of DR/WiFi/MM #2 errors was 3.0 m, which was 65.5% and 14.3% less than those of DR/WiFi/MM #0 and #1, respectively.

4.2. Results of test group #2

The testers walked along the path in Fig. 11(b) for several rounds. Two different types of tests were conducted. In Type #1, the smartphones were handheld horizontally during the whole test, while in Type #2, the users switched among handheld, phoning, dangling, and pocketed. Fig. 17(a) and (b) illustrate the gyro and accelerometer outputs during a Type #1 test and a Type #2 test, respectively. Color bars at the bottom of the figures indicate the motion conditions during the corresponding time periods.

Compared with Group #1 tests, Group #2 had four differences:

- The algorithm needed to initialize position and heading by using WiFi and magnetometers.
- In Type #2, changes of motion conditions might introduce a misalignment angle.
- The tests lasted for a longer time period (half an hour for Type #1, and an hour for Type #2).
- Out-of-dated WiFi and MM databases were used.

Figs. 18 and 19 illustrate results for a Type #1 and #2 test, respectively, in which (a) is for DR, and (b) – (d) are for three

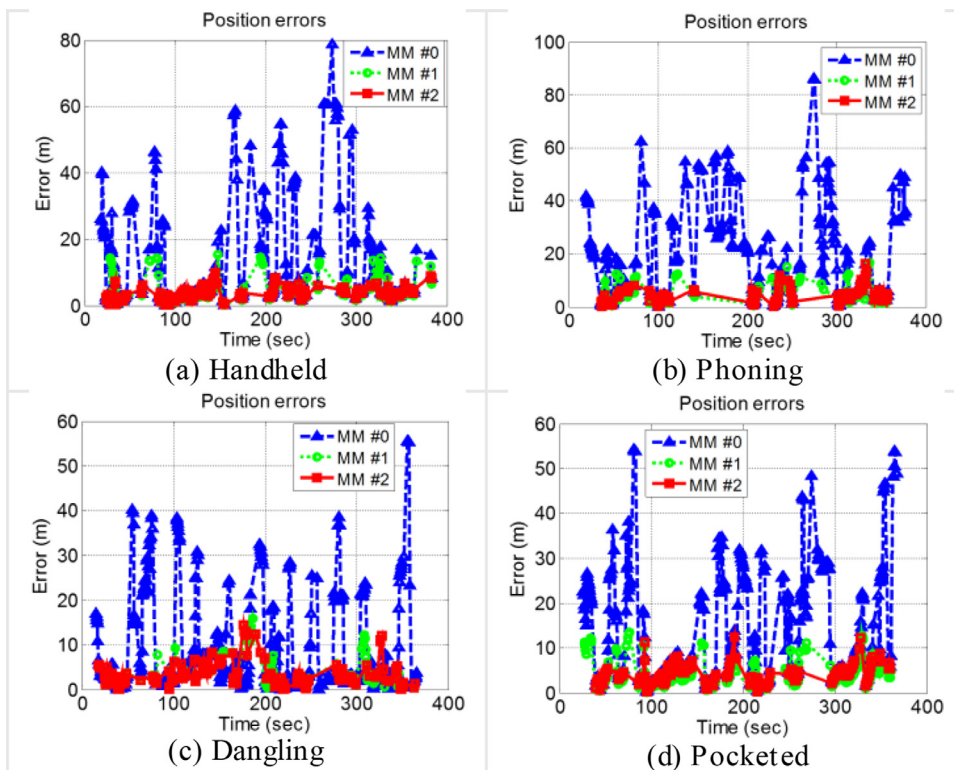


Fig. 14. Position errors of MM #0, #1, and #2 (Group #1).

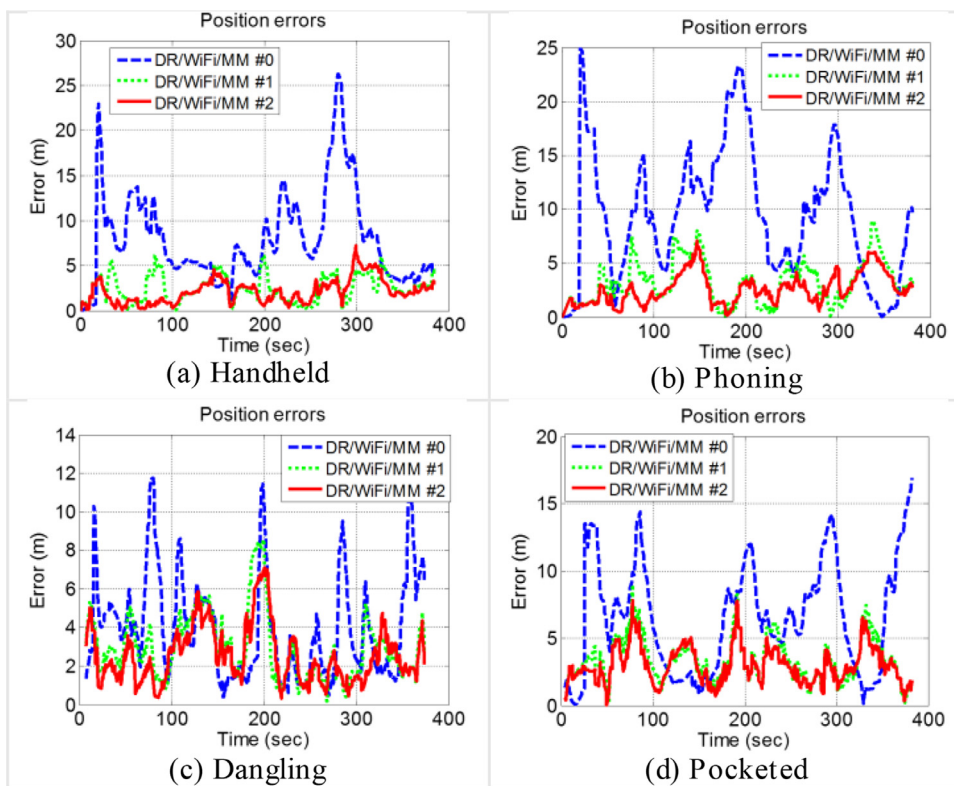


Fig. 15. Position errors of DR/WiFi/MM #0, #1, and #2 (Group #1).

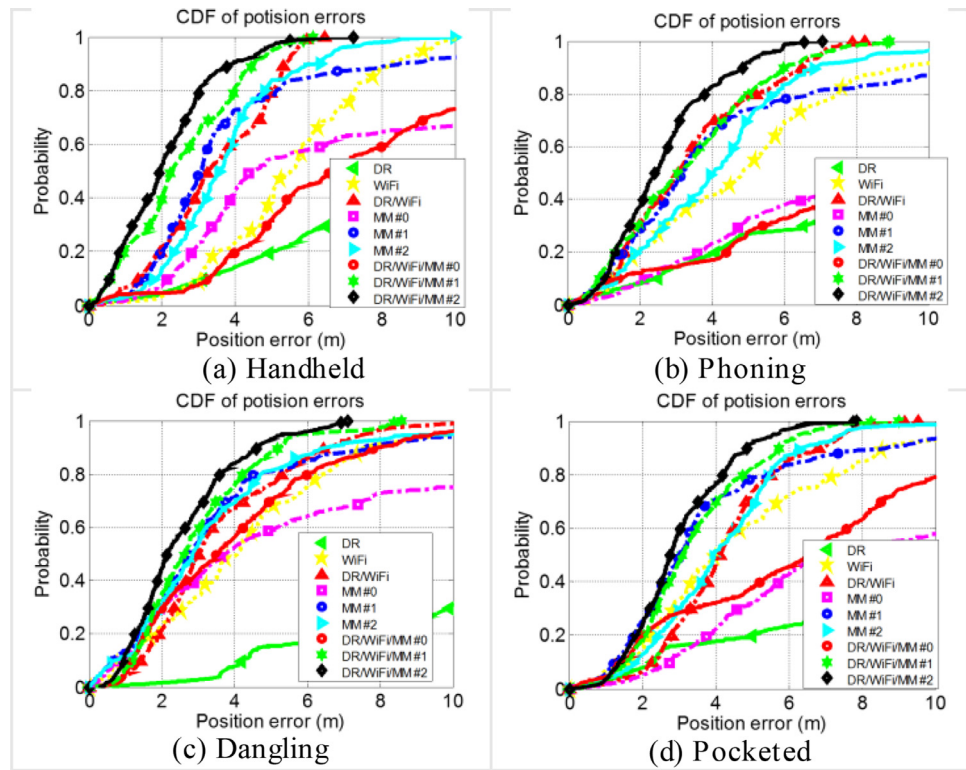


Fig. 16. CDF of position errors when using different strategies (Group #1).

Table 3
Statistical values of position errors and mismatch rates (Group #1).

Motion	Error	A**	B	C	D	E	F	G	H	I
Handheld	RMS	11.4	5.9	3.7	20.9	5.1	4.1	9.5	2.9	2.5
	80%	14.8	7.3	5.1	21.9	5.4	4.8	11.6	4.0	3.0
	M*(%)	18.5	0	0	17.6	0.2	0	6.5	0	0
Phoning	RMS	12.2	6.2	3.9	25.4	5.8	5.0	11.3	3.9	3.0
	80%	16.3	7.5	5.3	32.2	6.7	5.8	14.5	5.0	3.8
	M(%)	22.5	0.4	0	25.3	0.7	0.2	18.2	0	0
Dangling	RMS	17.2	5.2	4.2	13.7	4.7	4.5	4.9	3.4	3.0
	80%	22.9	6.5	5.3	17.0	5.8	4.8	6.1	4.2	3.6
	M(%)	42.9	0	0	15.7	0.2	0	0	0	0
Pocketed	RMS	24.4	5.6	4.6	18.2	4.8	4.6	7.7	3.7	3.3
	80%	24.1	7.5	5.5	24.6	5.4	5.4	10.4	4.8	4.2
	M(%)	44.1	0	0	24.5	0	0	1.6	0	0
General***	RMS	17.1	5.6	4.0	20.0	5.1	4.6	8.7	3.5	3.0
	80%	19.9	7.2	5.0	24.6	5.8	5.2	11.1	4.5	3.7
	M(%)	34.0	0.2	0	21.2	0.4	0.1	9.7	0	0

* M (%)- Mismatch rate (unit: percent)

** A-DR; B-WiFi; C-DR/WiFi; D-MM #0; E-MM #1; F-MM #2; G-DR/WiFi/MM #0; H-DR/WiFi/MM #1; I-DR/WiFi/MM #2

*** General - RMS of corresponding values under four motion conditions.

DR/WiFi/MM structures. Colors in Fig. 18 indicate seven rounds, while those in Fig. 19 represent four motion conditions.

Figs. 18 and 19 demonstrate that

- Figs. 18(a) and 19 (a) show the impact of the initialization issue and the occurrences of misalignment angle on DR. In Fig. 18(a), the initial heading error reached 130 deg. Meanwhile, in Fig. 19(a), a misalignment angle occurred when switching between motions, e.g., handheld and phoning.
- In Fig. 19(b), the DR/WiFi/MM #0 solution suffered from severer shape changes than the results in Group #1. This reason was probably that the performance of WiFi and MM was degraded due to the use of out-of-dated databases.

- When either DR/WiFi/MM #1 or #2 was used, navigation results became generally reliable. This outcome further supported the importance of QC in DR/WiFi/MM integration.
- In both Figs. 18(d) and 19 (d), solutions under the same motion condition had the similar shape. This phenomenon indicated the repeatability of the DR/WiFi/MM #2 solution. Meanwhile, in Fig. 19(d), solutions under various motion conditions had a similar accuracy level, which indicated the consistence of the DR/WiFi/MM #2 solution under different motion conditions.
- Compared with Fig. 19(d), the shape of the Fig. 18(d) result was closer to the true trajectory. This outcome can be explained as follows: in Type #1 tests, position errors increased gradually because there was no misalignment angle; thus, when WiFi

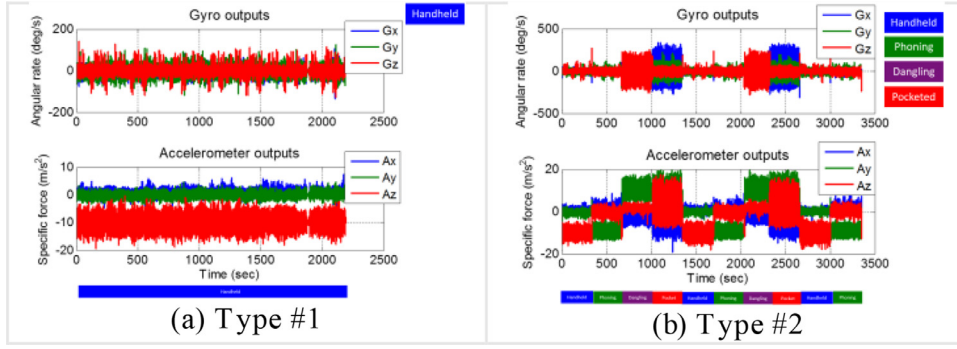


Fig. 17. Gyro and accelerometer signals in Type #1 and #2 tests (Group #2).

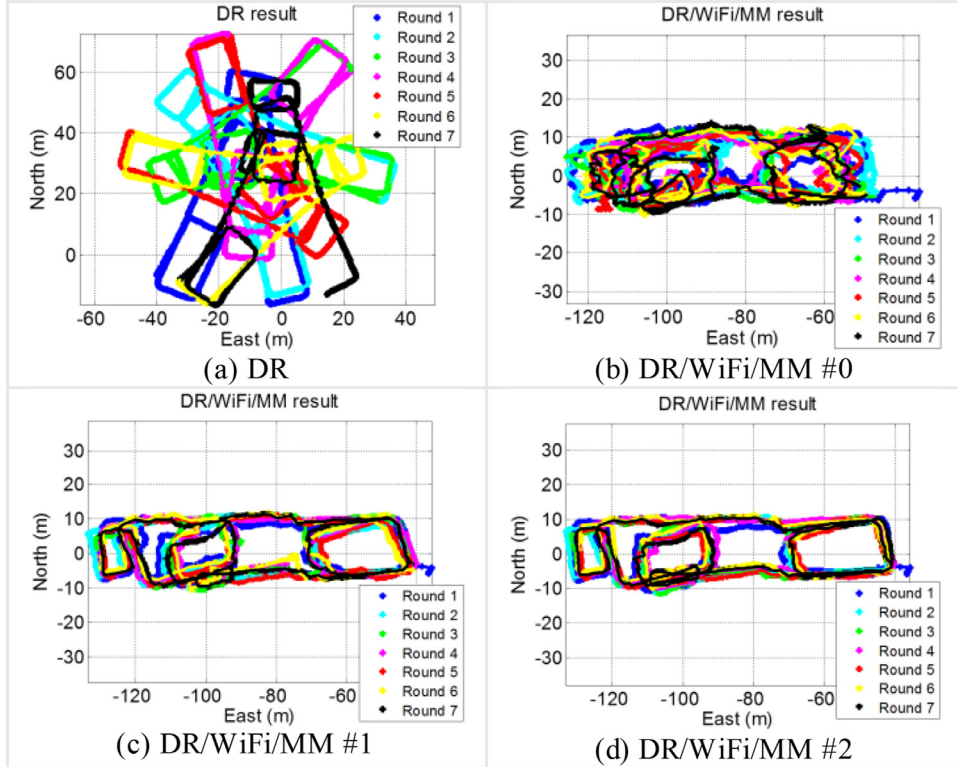


Fig. 18. DR and DR/WiFi/MM #0, #1, and #2 results (Type #1, Group #2).

and MM position updates were available, the integration results became reliable in long term. On the other hand, in Type #2 tests, DR errors might increase suddenly due to the occurrence of misalignment; thus, the integration results were vulnerable to degradations when the WiFi and MM positions were not accurate. However, even with out-of-dated databases and motion changes, both DR/WiFi/MM #1 and #2 solutions were smooth and had similar shapes to the true trajectory.

Figs. 20(a) and (b) show position errors for three DR/WiFi/MM structures in a Type #1 and #2 test, respectively.

Fig. 20 shows that:

- In Type #1, DR/WiFi/MM #1 and #2 provided similar results;
- In Type #2, the DR/WiFi/MM #2 result was more accurate. Position errors at 1000 s and 3000 s were reduced.

Fig. 21 illustrates the CDF curves of position errors, and Figs. 22 and 23 illustrate the RMS values of position errors and the mismatch rates of Group #1 and #2 results, respectively. Table 4 compares the statistical values of errors and the mismatch rates in Type #1 and #2 tests.

Figs. 21–23 and Table 4 illustrate that

- Accuracy and mismatch rate are two related indicators, but not exactly the same. For example, in Type #2, DR/WiFi/MM #1 results had a smaller RMS of position errors (6.4 m) than WiFi (7.0 m) but suffered from a higher mismatch rate (2.1%).
- In Type #1, DR/WiFi results had a smaller mismatch rate than WiFi because DR solutions drifted gradually. Contrarily, in Type #2, DR/WiFi solutions had a larger mismatch rate, which indicated that the introduction of DR increased the risk of degradation of solutions. Thus, a reliable multi-sensor integration structure is important.
- In Type #1, both DR/WiFi/MM #1 and #2 results did not have any mismatch, and has similar accuracy. However, in the challenging Type #2 tests, DR/WiFi/MM #2 reduced the mismatch rate from 2.1% to 0.6% when compared with DR/WiFi/MM #1; meanwhile, the RMS of position errors reduced from 6.4 m to 5.4 m.

DR/WiFi/MM #2 solutions had both the smallest RMS value and the lowest mismatch rate. The DR/WiFi/MM #2 performance was

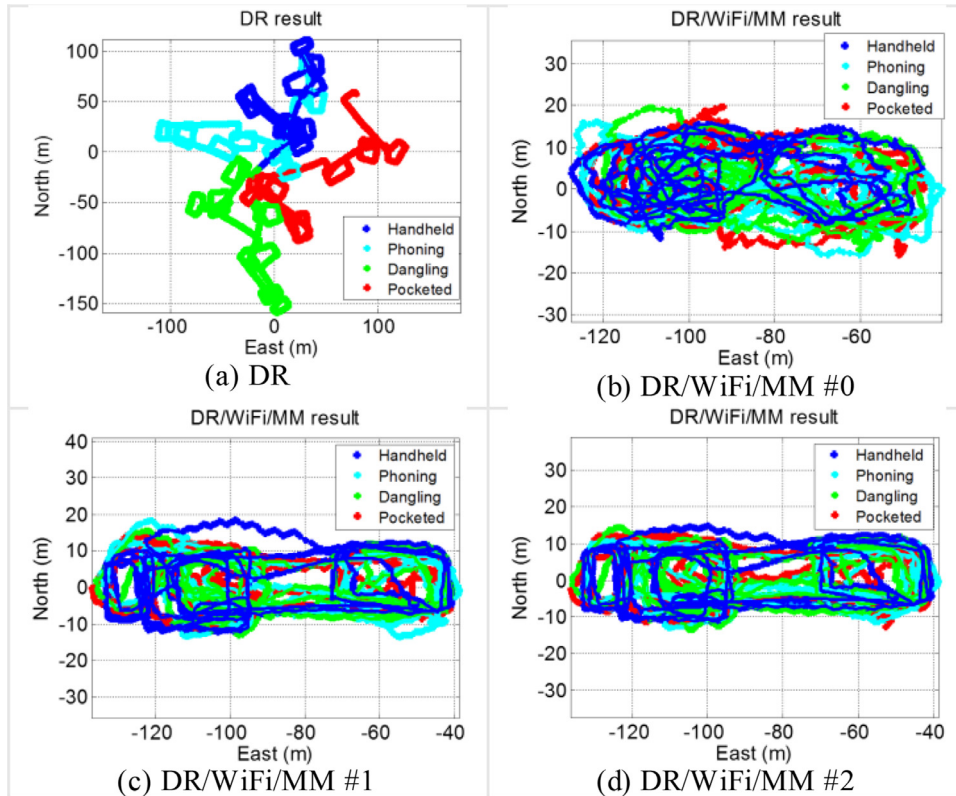


Fig. 19. DR and DR/WiFi/MM #0, #1, and #2 results (Type #2, Group #2).

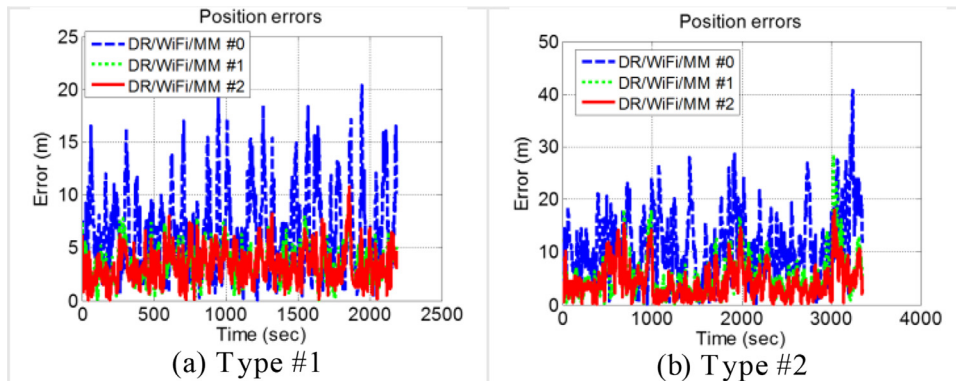


Fig. 20. Position errors of DR/WiFi/MM #0, #1, and #2 in a Type #1 and #2 test (Group 2).

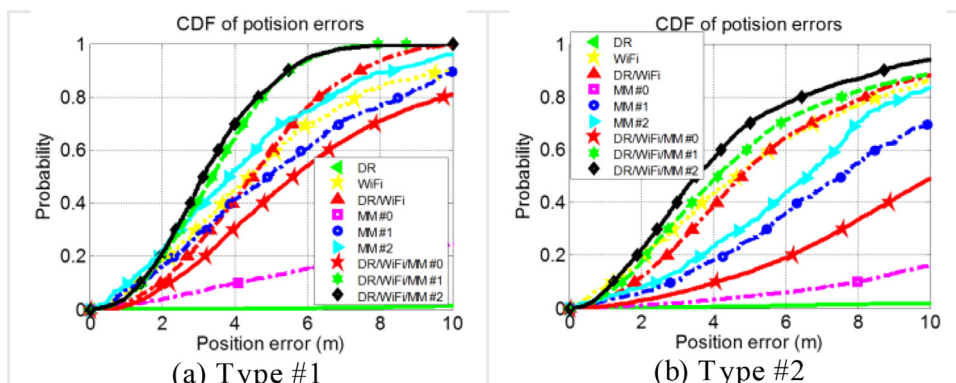


Fig. 21. CDF of position errors when using different strategies for Type #1 and Type #2 tests (Group #2).

Table 4
Statistical values of position errors and mismatch rates (Group #2).

Type	Error	A	B	C	D	E	F	G	H	I
#1	RMS	41.2	6.3	5.0	26.1	6.4	5.1	7.6	3.8	3.7
	80%	52.9	7.4	6.3	35.0	8.6	6.6	9.8	4.8	4.7
	M(%)	95.5	0.3	0	42.0	0.2	0	3.7	0	0
#2	RMS	130.4	7.0	7.1	27.0	9.2	7.6	12.8	6.4	5.4
	80%	164.9	8.7	8.2	33.6	11.8	9.4	16.4	7.6	6.5
	M(%)	96.3	0.7	3.3	42.6	0.8	0.2	29.4	2.1	0.6

A-DR; B-WiFi; C-DR/WiFi; D-MM #0; E-MM #1; F-MM #2; G-DR/WiFi/MM #0; H-DR/WiFi/MM #1; I-DR/WiFi/MM #2

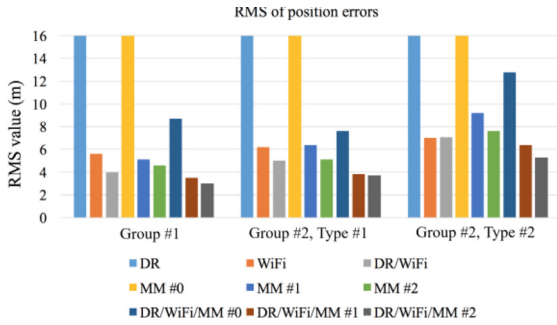


Fig. 22. RMS values of position errors in Groups #1 and #2 (values beyond 16 m are not shown).

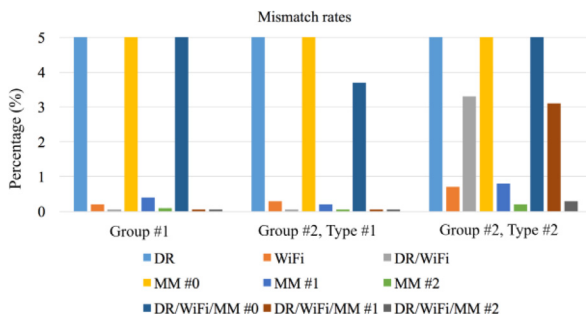


Fig. 23. Mismatch rates of results in Groups #1 and #2 (values beyond 5% are not shown).

promising when considering that the tests were implemented with low-cost sensors, existing WiFi infrastructures, and out-of-dated databases generated through quick walk-survey, and there were motion changes during the tests.

4.3. Results of test group #3

Group #3 tests were conducted to evaluate the navigation performances in areas with various WiFi and magnetic distributions. [Fig. 24](#) illustrates the results of one handheld test at Building #2 as examples.

Solutions at Building #2 generally had similar characteristics to those at Building #1. A difference was that MM results at Building #2 were sparser. The reason for this outcome was that the magnetic intensity changes were not significant at Building #2; thus, more MM results were removed on QC Level #1. [Figs. 25\(a\) - \(d\)](#) provide the CDF curves of position errors from different strategies, and [Table 5](#) illustrates the statistical values of errors.

[Fig. 25](#) and [Table 5](#) illustrate that in Group #3 tests:

- DR/WiFi/MM #1 results had a smaller RMS (4.8 m) of position errors than DR/WiFi (5.7 m). However, because there were mismatches remaining in MM #1 results, DR/WiFi/MM #1 results suffered from a mismatch rate of 0.2%, while DR/WiFi did not have any mismatch.
- The use of DR/WiFi/MM #2 removed the mismatches which occurred when using the other integration structures, and reduced the RMS of position errors from 4.8 m to 4.3 m (improved by 10.4%). Thus, DR/WiFi/MM #2 provided the most accurate and reliable navigation solutions at Building #2.

[Figs. 26](#) and [27](#) show the RMS values of position errors and mismatch rates of results at Buildings #1 and #2, respectively.

[Tables 3–5](#) and [Figs. 26](#) and [27](#) illustrate that:

- The accuracy of each single technology may impact the whole integration system. For example, the RMS of WiFi position errors (7.2 m) at Building #2 was 26.3% larger than that at Building #1 (5.7 m). Accordingly, the RMS values of DR/WiFi, MM#1, and MM #2 errors (5.9 m, 7.2 m, and 7.3 m) at Building #2 were 18%, 25.9%, and 26.9% larger than those at Building #1 (5.0 m, 5.8 m, and 5.2 m), respectively.

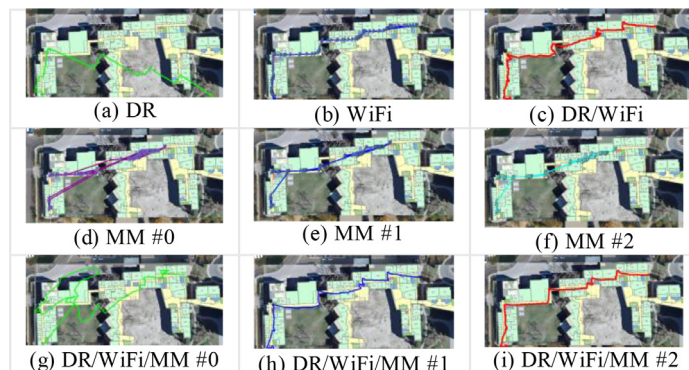


Fig. 24. Position results at Building #2 (handheld).

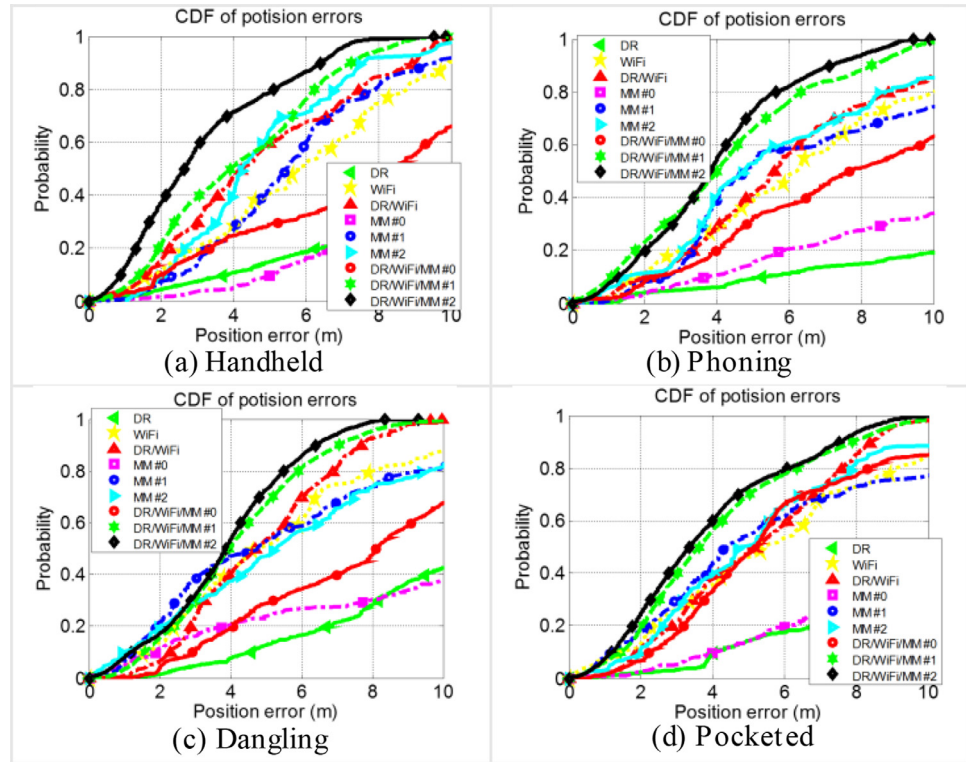


Fig. 25. CDF of position errors when using different strategies (Group #3).

Table 5
Statistical values of position errors and mismatch rates (Group #3).

Motion	Error	A	B	C	D	E	F	G	H	I
Handheld	RMS	16.3	6.7	5.5	22.5	6.6	5.3	10.0	4.7	3.7
	80%	22.7	8.4	7.5	24.3	7.9	6.8	12.8	6.2	5.1
	M(%)	47.7	0	0.2	21.3	0.3	0	10.9	0	0
Phoning	RMS	22.4	7.8	6.7	24.1	8.0	7.1	9.9	5.0	4.5
	80%	26.1	9.8	8.9	28.6	11.2	8.8	13.1	6.3	5.7
	M(%)	65.2	2.1	1.4	26.6	0.9	0.5	12.2	0	0
Dangling	RMS	15.7	6.5	5.3	21.5	7.3	7.1	9.8	4.7	4.3
	80%	17.6	8.3	6.9	27.7	9.5	9.6	12.6	5.9	5.5
	M(%)	27.6	1.6	0.3	27.3	2.2	0.8	14.4	0.3	4.1
Pocketed	RMS	20.4	7.7	5.8	17.7	7.4	6.7	6.9	4.8	4.5
	80%	21.9	9.2	7.6	22.5	11.0	7.9	8.4	6.4	6.1
	M(%)	40.4	1.8	1.6	25.2	0.9	0.7	0.3	0.2	0
General	RMS	17.7	7.2	5.9	21.6	7.3	6.6	9.2	4.8	4.3
	80%	2.3	8.9	7.7	25.9	10.0	8.3	11.9	6.2	5.6
	M(%)	47.2	1.6	1.1	25.2	1.3	0.6	10.9	0.2	0

A-DR; B-WiFi; C-DR/WiFi; D-MM #0; E-MM #1; F-MM #2; G-DR/WiFi/MM #0; H-DR/WiFi/MM #1; I-DR/WiFi/MM #2

- The impact of environment was mitigated when more technologies were used. The differences between the RMS values of position errors at Buildings #1 and #2 were 0.6 m, 0.5 m, and 0.7 m for DR/WiFi/MM #1, #2, and #3, respectively. These values were smaller than the differences for DR (33.5 m), WiFi (1.0 m), DR/WiFi (0.8 m), MM #0 (2.2 m), MM #1 (1.6 m), and MM #2 (1.3 m).
- However, the use of more technologies increased the risk of mismatches in some tests (e.g., DR/WiFi results had a higher mismatch rate than WiFi at Building #1), but reduced the mismatch rate when considering the overall results under all scenarios comprehensively. DR/WiFi provided more reliable result ($M_{\max} = 1.1\%$) than WiFi ($M_{\max} = 1.6\%$), and MM #2 provided more reliable results ($M_{\max} = 0.6\%$) than MM #1 ($M_{\max} = 1.3\%$). Especially, DR/WiFi/MM #2 results had the lowest mismatch

rate ($M_{\max} = 0.3\%$) among the nine strategies, which was 75.0% and 97.0% smaller than DR/WiFi/MM #0 ($M_{\max} = 1.2\%$) and #1 (M_{\max} was over 10%), respectively. M_{\max} represents the maximum mismatch rate in all tests.

5. Conclusions

This paper presents an improved dead-reckoning (DR)/WiFi fingerprinting/magnetic matching (MM) integration structure. The proposed structure was compared with two previous DR/WiFi/MM integration structures through tests that considered challenging issues such as the initialization of navigation, the changes of motion conditions, and the timeliness of databases. Besides accuracy, the mismatch rate (i.e., the percentage of the positioning results that have position errors of over 15 m) is introduced as an indica-

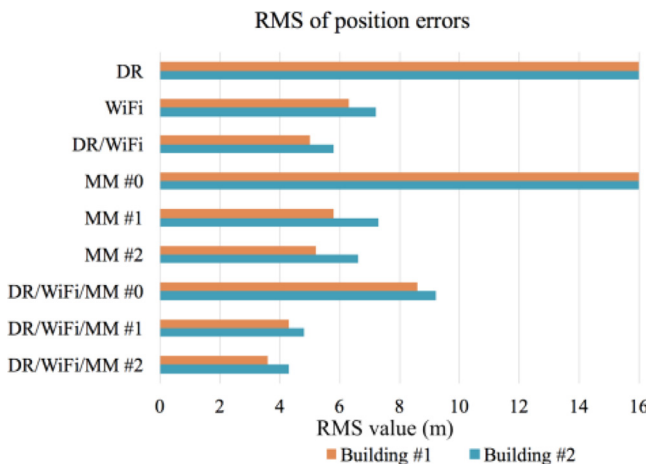


Fig. 26. RMS values of position errors in two environments (values beyond 16 m are not shown).

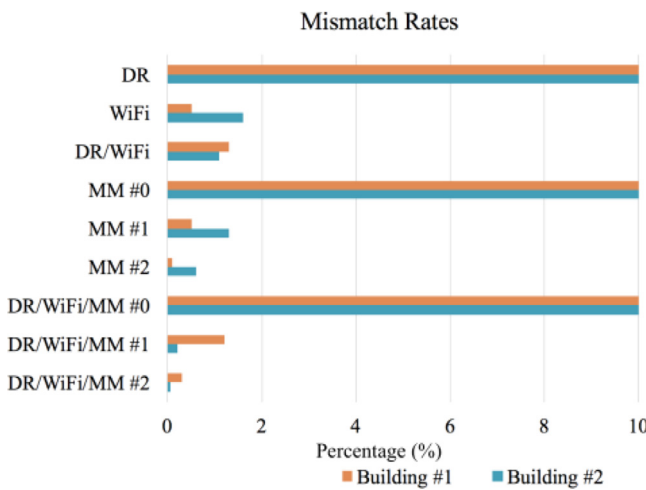


Fig. 27. Mismatch rates of navigation solutions in two environments (values beyond 10% are not shown).

tor to evaluate the reliability. The proposed DR/WiFi/MM #2 structure provided results that had smaller root mean square (RMS) of position errors (3.5 m and 4.3 m in two environments) than the previous DR/WiFi/MM #0 (8.5 m and 9.1 m) and #1 (4.3 m and 4.8 m) structures, and had lower mismatch rate ($M_{\max} = 0.3\%$) than DR/WiFi/MM #0 ($M_{\max} = 1.2\%$) and #1 ($M_{\max} > 10\%$). M_{\max} represents the maximum mismatch rate in all tests. It was also found that the introduction of more techniques might increase the risk of mismatches and degrade the robustness of the overall navigation system. This outcome indicates the importance of the information fusion technique, as various integration structures led to significantly different results.

Future works will focus on quantitative investigations on contributions of different techniques in DR/WiFi/MM integration and criteria for evaluating the robustness of integrated navigation systems. Also, navigation in a multi-floor building will be researched.

Acknowledgments

The authors would like to thank the anonymous reviewers and the Editor for their valuable comments and suggestions. This work was supported in part by National Natural Science Foundation of China (41174028 and 41304004), the China Scholarship Council Foundation (201306270139), and the research funding from Dr. Naser El-Sheimy.

References

- [1] E.P. Herrera, H. Kaufmann, J. Secue, R. Quirós, G. Fabregat, Improving data fusion in personal positioning systems for outdoor environments, *Inf. Fusion* 14 (1) (2013) 45–56.
- [2] I.L. Dos Santos, L. Pirmez, É., T. Lemos, F.C. Delicato, L.A.V. Pinto, J.N. de Souza, et al., A localized algorithm for Structural Health Monitoring using wireless sensor networks, *Inf. Fusion* 15 (1) (2014) 114–129.
- [3] K.A. Rahim, Heading Drift Mitigation for Low Cost Inertial Pedestrian Navigation, The University of Nottingham, 2012 PhD.
- [4] M.F. Mokbel, J.J. Levandoski, Toward context and preference-aware location-based services, in: Proceedings of the Eighth ACM International Workshop on Data Engineering for Wireless and Mobile Access, 2009, pp. 25–32.
- [5] X. Li, J. Wang, T. Li, Seamless positioning and navigation by using Geo-referenced images and multi-sensor data, *Sensors* 13 (7) (2013) 9047–9069.
- [6] R. Mautz, Indoor Positioning Technologies, *Habil. ETH Zürich*, 2012 2012.
- [7] N. Fallah, I. Apostolopoulos, K. Bekris, E. Folmer, Indoor human navigation systems: a survey, *Interact. Comput.* 25 (1) (2013) 21–33.
- [8] J. Talvitie, M. Renfors, E.S. Lohan, Distance-based interpolation and extrapolation methods for RSS-based localization with indoor wireless signals, *IEEE Trans. Veh. Technol.* 64 (4) (2015) 1340–1353.
- [9] P. Bahl, V.N. Padmanabhan, RADAR: an in-building RF-based user location and tracking system, in: Nineteenth Annual Joint Conference of the IEEE Computer and Communications Societies, 2000, pp. 775–784.
- [10] Y. Cheng, X. Wang, M. Morelande, B. Moran, Information geometry of target tracking sensor networks, *Inf. Fusion* 14 (3) (2013) 311–326.
- [11] Y. Zhuang, Z. Syed, J. Georgy, N. El-Sheimy, Autonomous smartphone-based WiFi positioning system by using access points localization and crowdsourcing, *Pervasive Mob. Comput.* 18 (1) (2015) 118–136.
- [12] J. Torres-Solis, T.H. Falk, T. Chau, A review of indoor localization technologies: towards navigational assistance for topographical disorientation, *Ambient Intell.* (2010) 51–84.
- [13] A. Bose, C.H. Foh, A practical path loss model for indoor WiFi positioning enhancement, in: 6th International Conference on Information, Communications & Signal Processing, 2007, pp. 1–5.
- [14] C. Laoudias, D. Zeinalipour-Yazti, C.G. Panayiotou, Crowdsourced indoor localization for diverse devices through radiomap fusion, in: International Conference on Indoor Positioning and Indoor Navigation (IPIN), 2013, pp. 1–7.
- [15] D.K. Shaefi, MEMS inertial sensors: a tutorial overview, *IEEE Commun. Mag.* 51 (4) (2013) 100–109.
- [16] A.N. Ndjeng, D. Gruyer, S. Glaser, A. Lambert, Low cost IMU–Odometer–GPS ego localization for unusual maneuvers, *Inf. Fusion* 12 (4) (2011) 264–274.
- [17] D.H. Titterton, J.L. Weston, Strapdown Inertial Navigation Technology, 2nd ed., The Institution of Electrical Engineers, London, United Kingdom, 2004.
- [18] S. Bonnet, C. Bassompierre, C. Godin, S. Lesecq, A. Barraud, Calibration methods for inertial and magnetic sensors, *Sens. Actuators, A* 156 (2) (2009) 302–311.
- [19] X. Niu, Y. Li, H. Zhang, Q. Wang, Y. Ban, Fast thermal calibration of low-grade inertial sensors and inertial measurement units, *Sensors* 13 (9) (2013) 12192–12217.
- [20] X. Niu, Y. Li, Q. Zhang, Y. Cheng, C. Shi, Observability analysis of non-holonomic constraints for land-vehicle navigation systems, *J. Global Position. Syst.* 11 (1) (2012) 80–88.
- [21] R. Zhang, F. Hoflinger, L. Reindl, Inertial sensor based indoor localization and monitoring system for emergency responders, *IEEE Sens. J.* 13 (2) (2013) 838–848.
- [22] A. Chambodut, Geomagnetic field, IGRF, in: Encyclopedia of Solid Earth Geophysics, Springer, 2011, pp. 379–380.
- [23] B. Gozick, K.P. Subbu, R. Dantu, T. Maeshiro, Magnetic maps for indoor navigation, *IEEE Trans. Instrum. Meas.* 60 (12) (2011) 3883–3891.
- [24] K.P. Subbu, B. Gozick, R. Dantu, LocateMe: Magnetic-fields-based indoor localization using smartphones, *ACM Trans. Intell. Syst. Technol. (TIST)* 4 (4) (2013) 73.
- [25] J. Chung, M. Donahoe, C. Schmandt, I.-J. Kim, P. Razavai, M. Wiseman, Indoor location sensing using geo-magnetism, in: Proceedings of the 9th International Conference on Mobile Systems, Applications, and Services, 2011, pp. 141–154.
- [26] B. Gozick, K.P. Subbu, R. Dantu, T. Maeshiro, Magnetic maps for indoor navigation, *Instrument. Measur. IEEE Trans.* 60 (2011) 3883–3891.
- [27] J.P. Golden, Terrain contour matching (TERCOM): a cruise missile guidance aid, in: 24th Annual Technical Symposium, 1980, pp. 10–18.
- [28] L. Yan, C. Cui, A new algorithm of gravity matching aided navigation, Second International Conference on Spatial Information Technology, 2007 pp. 679529–679529–6.
- [29] Y. Liu, M. Wu, X. Hu, H. Xie, Research on geomagnetic matching method, in: 2nd IEEE Conference on Industrial Electronics and Applications, 2007, pp. 2707–2711.
- [30] B. Khaleghi, A. Khamis, F.O. Karray, S.N. Razavi, Multisensor data fusion: a review of the state-of-the-art, *Inf. Fusion* 14 (1) (2013) 28–44.
- [31] Q. Ladetto, V. Gabaglio, B. Merminod, Combining gyroscopes, magnetic compass and GPS for pedestrian navigation, in: Proceedings of the International Symposium on Kinematic Systems in Geodesy, Geomatics, and Navigation, 2001, pp. 205–213.
- [32] Y. Li, J. Georgy, X. Niu, Q. Li, N. El-Sheimy, Autonomous Calibration of MEMS Gyros in Consumer Portable Devices, *IEEE Sens. J.* 15 (7) (2015) 4062–4072.
- [33] Z. Tian, X. Fang, M. Zhou, L. Li, Smartphone-based indoor integrated WiFi/MEMS positioning algorithm in a multi-floor environment, *Micromachines* 6 (3) (2015) 347–363.

- [34] F. Evennou, F. Marx, Advanced integration of WiFi and inertial navigation systems for indoor mobile positioning, *Eurasip J. Appl. Sig. Process.* 2006 (1) (2006) 164.
- [35] A.R.J. Ruiz, F.S. Granja, J.C. Prieto Honorato, J.I.G. Rosas, Accurate pedestrian indoor navigation by tightly coupling foot-mounted IMU and RFID measurements, *IEEE Trans. Instrum. Meas.* 61 (1) (2012) 178–189.
- [36] B. Li, T. Gallagher, A.G. Dempster, C. Rizos, How feasible is the use of magnetic field alone for indoor positioning? in: *International Conference on Indoor Positioning and Indoor Navigation*, 2012, p. 15th.
- [37] H. Xie, T. Gu, X. Tao, H. Ye, J. Lv, MaLoc: a practical magnetic fingerprinting approach to indoor localization using smartphones, in: *Proceedings of the 2014 ACM International Joint Conference on Pervasive and Ubiquitous Computing*, 2014, pp. 243–253.
- [38] M. Ezani, M. Faheem, M.A. Abdullah, S. Haseeb, A region-to-point indoor localization approach via RSS-magnetic fingerprinting, in: *Information and Communication Technology for The Muslim World (ICT4M), 2014 The 5th International Conference on*, 2014, pp. 1–6.
- [39] Y. Shu, C. Bo, G. Shen, C. Zhao, and F. Zhao, "Magicol: indoor localization using pervasive magnetic field and opportunistic WiFi sensing," *IEEE J. Sel. Areas Commun.*, vol. 1, no. 1, pp. 1–14.
- [40] N. Pritt, Indoor navigation with use of geomagnetic anomalies, in: *2014 IEEE International Geoscience and Remote Sensing Symposium (IGARSS)*, 2014, pp. 1859–1862.
- [41] R. Ban, K. Kaji, K. Hiroi, N. Kawaguchi, Indoor positioning method integrating pedestrian Dead Reckoning with magnetic field and WiFi fingerprints, in: *Eighth International Conference on Mobile Computing and Ubiquitous Networking (ICMU)*, 2015, pp. 167–172.
- [42] P. Mirowski, T.K. Ho, S. Yi, M. MacDonald, Signalslam: simultaneous localization and mapping with mixed wifi, bluetooth, LTE and magnetic signals, in: *2013 International Conference on Indoor Positioning and Indoor Navigation (IPIN)*, 2013, pp. 1–10.
- [43] E.-H. Shin, Estimation Techniques for Low-Cost Inertial Navigation, Department of Geomatics Engineering, University of Calgary, Calgary, Canada, 2005 PhD Dissertation/Thesis.
- [44] R.G. Brown, P.Y.C. Hwang, *Introduction to Random Signals and Applied Kalman Filtering*, vol. 1, John Wiley & Sons, New York, 1992.
- [45] Y. Li, X. Niu, Q. Zhang, H. Zhang, C. Shi, An in situ hand calibration method using a pseudo-observation scheme for low-end inertial measurement units, *Meas. Sci. Technol.* 23 (10) (2012) 105104.
- [46] J.H. Wilkinson, F.L. Bauer, C. Reinsch, *Linear Algebra*, vol. 2, Springer, 2013.
- [47] X. Niu, Z. Gao, R. Zhang, Z. Chen, J. Dong, Micro-machined attitude measurement unit with application in satellite TV antenna stabilization, in: *Symposium Gyro Technology 2002*, Stuttgart, Germany, 2002, p. 2002.
- [48] A. Saxena, G. Gupta, V. Gerasimov, S. Ourselin, In use parameter estimation of inertial sensors by detecting multilevel quasi-static states, in: *Knowledge-Based Intelligent Information and Engineering Systems*, 2005, pp. 595–601.
- [49] E.-H. Shin, N. El-Sheimy, *Accuracy Improvement of Low Cost INS/GPS for Land Applications*, University of Calgary, Department of Geomatics Engineering, 2001.
- [50] R. Harle, A survey of indoor inertial positioning systems for pedestrians, *IEEE Commun. Surv. Tutor.* 15 (3) (2013) 1281–1293.
- [51] S.H. Shin, C.G. Park, J.W. Kim, H.S. Hong, J.M. Lee, Adaptive step length estimation algorithm using low-cost MEMS inertial sensors, in: *IEEE Sensors Applications Symposium*, 2007, pp. 1–5.
- [52] J. Wang, Q. Gao, Y. Yu, P. Cheng, L. Wu, H. Wang, Robust device-free wireless localization based on differential RSS measurements, *IEEE Trans. Indust. Electron.* 60 (12) (2013) 5943–5952.
- [53] D. Zhen, H. Zhao, F. Gu, A. Ball, Phase-compensation-based dynamic time warping for fault diagnosis using the motor current signal, *Meas. Sci. Technol.* 23 (5) (2012) 055601.
- [54] S.K. Pathapati, G. Brandon, D. Ram, LocateMe: Magnetic-fields-based Indoor localization using smartphones, *ACM Trans. Intell. Syst. Technol. (TIST)* 4 (4) (2013) 73.
- [55] J.-G. Wang, Test statistics in Kalman filtering, *Positioning* 1 (13) (2008).
- [56] A. Mohamed, K. Schwarz, Adaptive Kalman filtering for INS/GPS, *J. Geod.* 73 (4) (1999) 193–203.
- [57] R.C. Luo, C.-C. Chang, Multisensor fusion and integration: A review on approaches and its applications in mechatronics, *IEEE Trans. Ind. Inf.* 8 (1) (2012) 49–60.
- [58] InvenSense MPU-6500 Product Specification Revision 1.1. Available: <http://www.invensense.com/mems/gyro/mpu6500.html>.
- [59] G. Panahandeh, M. Jansson, Vision-aided inertial navigation based on ground plane feature detection, *IEEE/ASME Trans. Mechatron.* 19 (4) (2014) 1206–1215.
- [60] Y. Li, Y. Zhuang, H. Lan, P. Zhang, X. Niu, N. El-Sheimy, WiFi-aided magnetic matching for indoor navigation with consumer portable devices, *Micromachines* 6 (6) (2015) 747–764.